Chem Soc Rev

REVIEW ARTICLE

View Article Online
View Journal

Cite this: DOI: 10.1039/d5cs01375e

Squaraine dyes for biophotonics: sensing, imaging and theranostics

Sivaramapanicker Sreejith, * Chodoparambil Sanjay, Balaraman Vedhanarayanan and Ayyappanpillai Ajayaghosh *

Squaraines, a celebrated class of organic dyes known for their remarkable photophysical properties, particularly fluorescence behaviour in the near infrared (NIR) region, have emerged as versatile molecular tools in the domain of biophotonics. They offer unparalleled opportunities for molecular sensing, bioimaging and theranostics. This review delves into the unique capabilities of these dyes, spotlighting advances in design and functionalization that enable their application across diverse biological systems. The sensitivity of squaraine dyes in biomolecular recognition is highlighted for detecting proteins such as bovine serum albumin (BSA) and enzymes like chymotrypsin. The fluorescence changes in squaraine dyes that signal binding events facilitate quantitative biomarker detection with superior detection limits. These signal responses enhance the utility of squaraines in DNA labeling, viscosity sensing, real time optical probing and cellular bioimaging. Beyond proteins and nucleic acids, the reactivity of squaraine dyes towards nucleophiles enables their use as both colorimetric and fluorimetric probes for the detection of thiol-containing biomolecules, lipids and metabolites. The dynamic optical responses of squaraine derivatives towards molecular interactions, such as reversible metal-ion binding, thiol-mediated interactions leading to fluorescence turn-on, *etc.*, provide key insights into biochemical pathways. Innovative functionalization strategies and engineering of supramolecular assembly formation in squaraine derivatives further enhance their selectivity and signal modulations in complex biological systems. This review also highlights the emerging theranostic potential of squaraine dyes specifically for targeted therapeutic interventions and their chemical robustness for long-term bioimaging and diagnostics. The growing applications of squaraine-based functional materials in molecular sensing, bioimaging and theranostics pave the way for innovative advancements in diagnostics, personalized medicine and biomedical research.

Received 18th November 2025

DOI: 10.1039/d5cs01375e

rsc.li/chem-soc-rev

Introduction

Squaraines (SQs), a class of organic dyes distinguished by their intense absorption and emission properties in the near-infrared (NIR) region, have garnered significant attention for various applications.[1–3] These compounds are uniquely characterized by the presence of a central zwitterionic squaric acid core,[4] which is substituted by electron-rich aromatic groups at opposite corners of the four-membered ring.[5–7] This distinctive structural configuration imparts exceptional photophysical properties to SQs, including high molar absorptivity, photostability and substantial fluorescence quantum yields.[8,9] Such chemical and physical attributes of SQs are exceptionally suitable for applications in organic electronics,[10] optical data storage, molecular sensing,[11] optical probes for bioimaging,[12–16] diagnostics,[17–19] catalysis, drug delivery,[20] *etc.*[21–23]

Department of Chemistry, SRM Institute of Science and Technology, Kattankulathur, Chennai, 603203, India. E-mail: ajayagha@srmist.edu.in, sreejits@srmist.edu.in

The absorption and emission features of SQs can be fine-tuned by altering their chemical structures.[24,25] This structural tunability allows for the customization of the properties of SQs for specific applications, ensuring optimal performance in various specialized tasks. For example, SQs exhibit narrow absorption in the NIR region of the spectrum with remarkable stability and relatively higher quantum yield under prolonged light exposure.[26,27] In 2008, we have reviewed the significant advancements in the chemistry of squaraine dyes, emphasizing their strong photophysical properties and potential applications in electronic and photonic devices.[5,28] This review underscored the importance of structural variations in squaraine dyes and how to tailor photophysical properties suitable for various technological applications.[5]

Fast forward to 2026, squaraine dye chemistry has continued to achieve substantial progress in addressing earlier limitations such as chemical instability and self-aggregation, especially under biological conditions.[29–31] Several studies have focused on enhancing the biocompatibility and photostability of these

dyes, expanding their applications in bioimaging and theranostics.[32–34] As the field of biophotonics rapidly evolves, it becomes imperative to consolidate and evaluate the progress made especially with a focus on squaraine dyes that have shown immense potential in various biomedical applications.[2] Given the increasing demand for non-invasive diagnostic tools and targeted therapy agents, it is crucial to understand the underlying mechanism, advantages, and limitations of these dyes in biological contexts.

In this review, we not only provide a critical analysis of the advancements in the design and applications of squaraine dyes but also identify emerging trends and future research directions. By customizing the composition of electron-donating or electron-withdrawing groups attached to the squaraine core, the photophysical properties of these dyes can be fine-tuned to respond specifically to molecular targets.[35] This approach makes them ideal NIR probes for biosensing applications. Similarly, due to their strong and narrow NIR absorption and

Sivaramapanicker Sreejith

Dr Sivaramapanicker Sreejith is an Assistant Professor of Chemistry at the SRM Institute of Science and Technology (SRMIST), Chennai, India. He received his PhD in Chemistry (2010) from CSIR-NIIST, Thiruvananthapuram under the mentorship of Prof. A. Ajayaghosh and pursued postdoctoral research as an Alexander von Humboldt Fellow in Germany (2010–2011). Subsequently, he served as a Research Fellow at Nanyang Technological University, Singapore (2011–2017) and as a Senior Research Fellow at the National University of Singapore (2017–2019). Later, he was appointed as an ad hoc faculty member at Mahatma Gandhi University, Kottayam (2020–2022) and subsequently as a Visiting Faculty member at the Department of Polymer Science and Rubber Technology, Cochin University of Science and Technology (2022–2024). He currently leads research activities in the domain of bio-nano systems at the Soft Materials Laboratory, Department of Chemistry, SRMIST, exploring the chemistry of functional organic materials and nanomaterials for diverse applications.

Chodoparambil Sanjay

Mr Chodoparambil Sanjay obtained his M Sc degree in Chemistry (2023) from Baselius College, Kottayam, India. Currently, he is a PhD student working under the guidance of Dr S. Sreejith at the Department of Chemistry, SRMIST. His research is on the design and development of functional molecular materials towards applications in biophotonics.

Balaraman Vedhanarayanan

Dr Balaraman Vedhanarayanan is an Assistant Professor and group leader of the 'Hybrid Materials and Energy Programme' of the Soft Materials Laboratory, Department of Chemistry, SRM Institute of Science and Technology, Kattankulathur, Chengalpattu, Tamilnadu, India. He completed his PhD in 2017 at CSIR-NIIST, Thiruvananthapuram under the mentorship of Prof. A. Ajayaghosh and worked as a Japan Society for the Promotion of Science (JSPS) fellow at Chiba University, Japan from 2022 to 2024. His research focuses on organic–inorganic functional hybrid materials for energy conversion and storage, integrating supramolecular chemistry, 2D materials, and electrochemistry.

Ayyappanpillai Ajayaghosh

Dr Ayyappanpillai Ajayaghosh is a Bhatnagar Chair Professor and CSIR Bhatnagar Fellow at the SRM Institute of Science and Technology, Chennai and is the former Director of CSIR-NIIST, Thiruvananthapuram, India. He obtained his PhD from Calicut University, India under the supervision of Prof. V. N. R. Pillai. His research is focussed on organic functional materials such as supramolecular materials, organogels, molecular probes and 2D polymers. He is a fellow of various national science academies of India and a fellow of TWAS and is a recipient of the Bhatnagar prize, the Infosys prize and the TWAS chemistry prize.

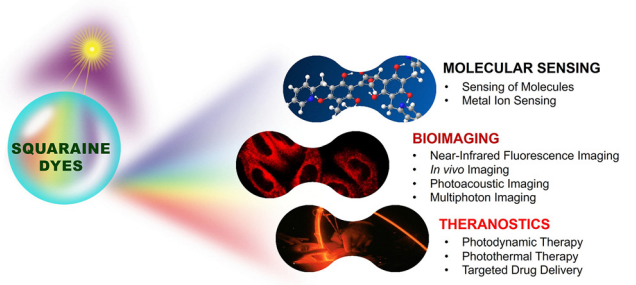

Fig. 1 Summary of biophotonic applications of squaraine derivatives across three main domains.

emission properties, several approaches have been explored, including encapsulation of the dyes inside nanoparticles and micelles,[36] conjugating them with biomolecules, *etc.* These strategies make squaraine dyes highly suitable as contrast agents for NIR-fluorescence imaging,[37] multi-photon imaging[38,39] and photoacoustic imaging.[40,41] Additionally, the dual-purpose capability of squaraines allows precise diagnosis through high-resolution imaging[42] and targeted therapeutic interventions.[43]

Our aim is to present a critical overview of the squaraine dye chemistry, emphasizing selected probes to illustrate recent advances at the frontiers of biophotonics applications. By bridging the gap between fundamental understanding and recent advancements, this review deep dives into the potential of squaraine dyes in biophotonics and inspires further exploration in this exciting research area (Fig. 1).

Structural chemistry and synthesis of squaraines

Core structure and functional groups

The core structure of squaraine dyes is based on squaric acid, specifically the 3,4-dihydroxycyclobut-3-ene-1,2-dione framework, which serves as a versatile platform for the synthesis of extended derivatives.[44,45] This structure allows the incorporation of diverse substituents that can significantly influence the photophysical properties of the resulting dyes.[46] The addition of electron-donating or electron withdrawing groups changes the π-electron distribution within the molecule, which in turn influences its absorption and emission properties.[47] In the dye structure, the central squaraine core acts as an acceptor unit, where 1,3 positions are occupied by electron rich aromatic units or heterocyclic rings. This feature facilitates strong intramolecular charge transfer (ICT) upon excitation, leading to stabilized charge-separated excited states.[48] Additionally, the π-conjugation between the electron rich and electron-deficient units enhances the ICT, resulting in sharp and intense absorption bands in the NIR region with high molar absorption coefficients ($\varepsilon \cong 10^5$ M^{-1} cm^{-1}).[48,49] However, squaraine chromophores are prone to solvent-induced aggregation, particularly in polar solvents and under biological conditions.[50] Such aggregation can significantly impact the favourable electronic transitions essential for biophotonics applications,[51] including intense near-IR and short-wave

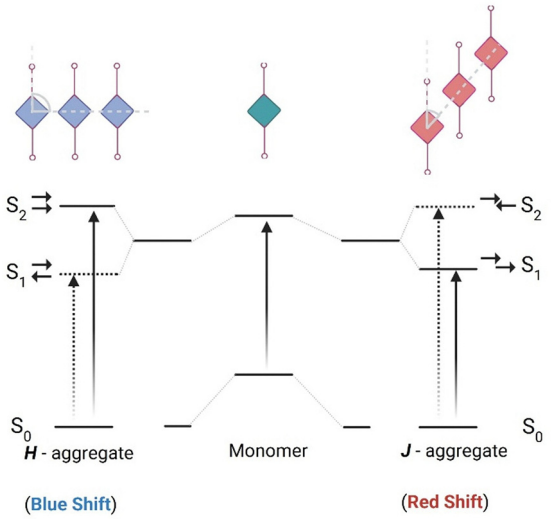

Scheme 1 Schematic representation of electronic transitions and the resulting spectral shifts in various molecular aggregates formed by squaraine derivatives.[55,56]

absorption and emission properties.[49] For instance, molecular packing within nearby chromophores can lead to the formation of H-aggregates[52] and J-aggregates,[53] resulting in blue-shift and red-shift in the absorption peaks, respectively (Scheme 1).[54–57] In squaraines, these electronic coupling processes are intense, causing delocalization of excited states over several units. These specific interactions result in large spectral shifts in the photophysical properties, with varying radiative and non-radiative characteristics. Various strategies have been implemented to prevent aggregation in squaraines, such as encapsulation in a macrocycle,[58,59] micelle inclusion of dyes,[60,61] nanomaterial loading,[62] *etc.*, for fluorescence bioimaging studies. Similarly, self-assembly of squaraine dyes[63] is found to be a promising approach for the design of photosensitizers for various therapeutic applications.[64]

Synthetic strategies

The synthesis of squaraine dyes involves a condensation reaction between squaric acid and various electron-rich aromatic compounds (Scheme 2).[2] This reaction is typically conducted by azeotropic condensation of aromatic hydrocarbons in high boiling alcohols.[65] The dye generally forms as a condensation product, with water being the only byproduct, which is removed *in situ*. The use of economical reaction conditions, less expensive reagents, easy separation and purification processes, and by product removal by distillation are some of the key advantages of squaraine synthesis. A straightforward synthetic approach with a 1 : 2 mole ratio can be adopted for the synthesis of 1,3-symmetrically substituted squaraine dyes. However, an alternative pathway for substitution, following an unsymmetrical route, involves a two-step synthetic process:[66] first, condensation reaction with an electron rich unit and squaric acid to form a semi-squaraine, which then can be reacted with another nucleophile to yield unsymmetrical dye analogues.[67] This unsymmetrical option

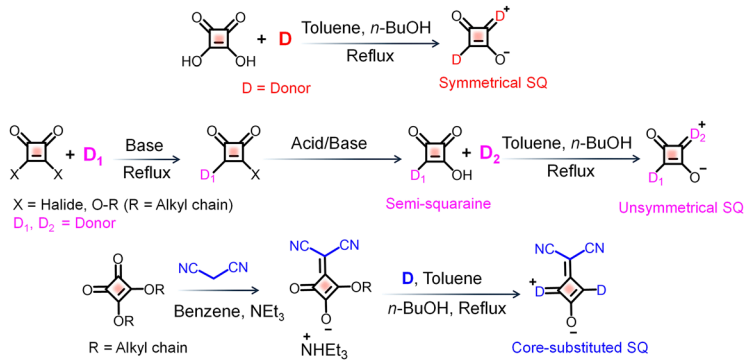

Scheme 2 Synthetic strategies for the preparation of squaraine (**SQ**) derivatives.[65]

of substitution in squaraine derivatives offers flexibility in dye design and tuning of photophysical properties suitable for biological conditions.[67]

Interestingly, by modifying the squaraine core with electron withdrawing substituents the optical properties of these dyes can be further tuned. Thus, the core substitution with a dicyanovinyl group *via* replacement of oxygen in the squaraine core generates another series of squaraine derivatives with impressive properties.[68] Synthesis of dicyano-functionalized squaraine derivatives could be achieved through a condensation reaction with malononitrile, followed by reactions with different electron rich moieties.[69] Such synthetic strategies enable the fine-tuning of the dyes' absorption and emission properties, which are critical for their performance in biophotonic applications. Variations in synthetic approaches, such as altering reaction conditions or employing different electron-rich partners, can lead to significant changes in the resulting squaraine dyes' properties.[70]

One of the significant challenges of using squaraine dyes for biological applications is their lack of solubility under aqueous conditions.[71,72] For instance, the introduction of specific functional groups on the electron rich segment of the dye can enhance solubility in aqueous environments, which is particularly important for biological applications.[73] Strategies to improve their water solubility and reduce cytotoxicity include incorporating hydrophilic groups and using carrier systems. For example, the attachment of polyethylene glycol (PEG) chains[69] or the formation of nanoparticles can significantly increase the solubility of squaraine dyes in aqueous media, making them more suitable for biological applications. Additionally, modifications aimed at targeting specific cellular components can enhance the therapeutic efficacy of squaraine dyes as well.

Photophysical and photochemical properties

Absorption and emission in the NIR region

Squaraine dyes are distinguished by their unique ability to absorb and emit light in the NIR region, typically between 700 nm and 900 nm (first biological window 680–950 nm).[74,75] This spectral range is particularly advantageous for various applications, especially in biomedical imaging and phototherapy, due to the reduced scattering and absorption by biological tissues at these wavelengths.[76,77] The mechanisms underlying NIR absorption and emission in squaraine dyes primarily involve intramolecular charge transfer (ICT) processes, where the electronic excitation occurs from a donor moiety (D) to an acceptor moiety (A) within the dye structure itself.[78] The advantages of NIR absorption include deeper tissue penetration, which is crucial for *in vivo* imaging applications.[18] For instance, squaraine dyes have been shown to exhibit high molar absorptivity, making them effective for low-concentration applications in biological systems.[79] Additionally, the narrow and intense absorption bands of squaraine dyes allow for specific targeting and imaging of biological markers, enhancing the sensitivity and specificity of fluorescence-based detection methods.[80] By engineering the strength of donor and acceptor moieties, recent studies have demonstrated the development of NIR-II active probes (Fig. 2).[81] The NIR-II region (1000–1700 nm) can reduce light scattering significantly and thus improve spatio-temporal resolution and deep tissue penetration for *in vivo* applications.[16] Moreover, the photochemical stability of squaraine dyes in the NIR region is noteworthy.[82] These dyes exhibit minimal photobleaching compared to traditional fluorescent dyes, which is essential for long-term imaging applications.[83] The ability to maintain fluorescence over extended periods allows for dynamic studies of biological processes without the interference of dye degradation.[84] By overcoming the limitations of light scattering and photobleaching, squaraine dyes have established significant milestones in biological applications (Fig. 2).[4,11–20]

Another favourable property of squaraine dyes for bioimaging applications is their high molar absorptivity, which often exceeds 10^5 M^{-1} cm^{-1}. This characteristic allows for effective excitation of the dye with minimal light intensity, reducing potential photodamage to biological samples.[64] The intense absorption in the NIR region (Fig. 3) enables the use of lower concentrations of the dye, which is particularly beneficial in minimizing background fluorescence and improving signal-to-noise ratios in imaging studies.[85] In addition to high molar absorptivity, squaraine dyes exhibit remarkable photostability, which is vital for long-term bioimaging.[86] Studies have demonstrated that squaraine dyes can retain their fluorescence intensity over extended periods, even when exposed to high-energy light

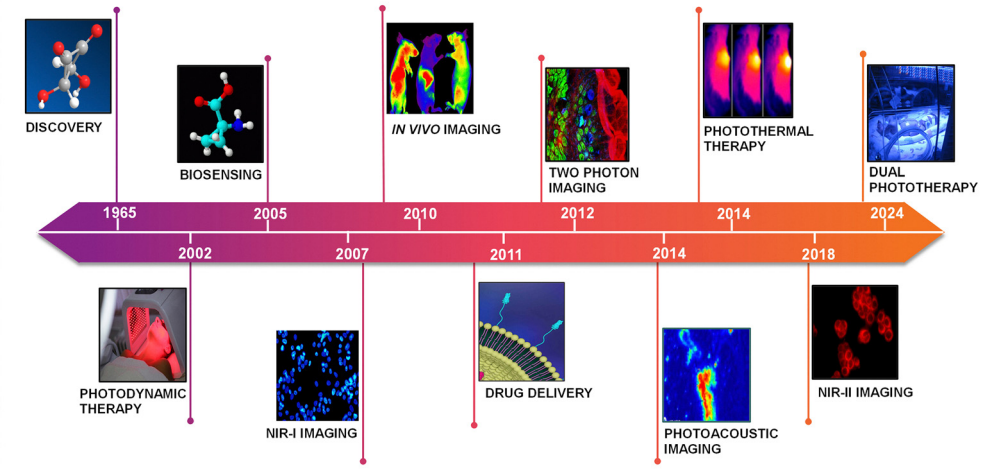

Fig. 2 Bio-applications of **SQ** dyes: key milestones and progress during 1965 (ref. 4), 2002 (ref. 17), 2005 (ref. 11), 2007 (ref. 12), 2010 (ref. 13), 2011 (ref. 20), 2012 (ref. 14), 2014 (ref. 15 and 18), 2018 (ref. 16), and 2024 (ref. 19) time frames.

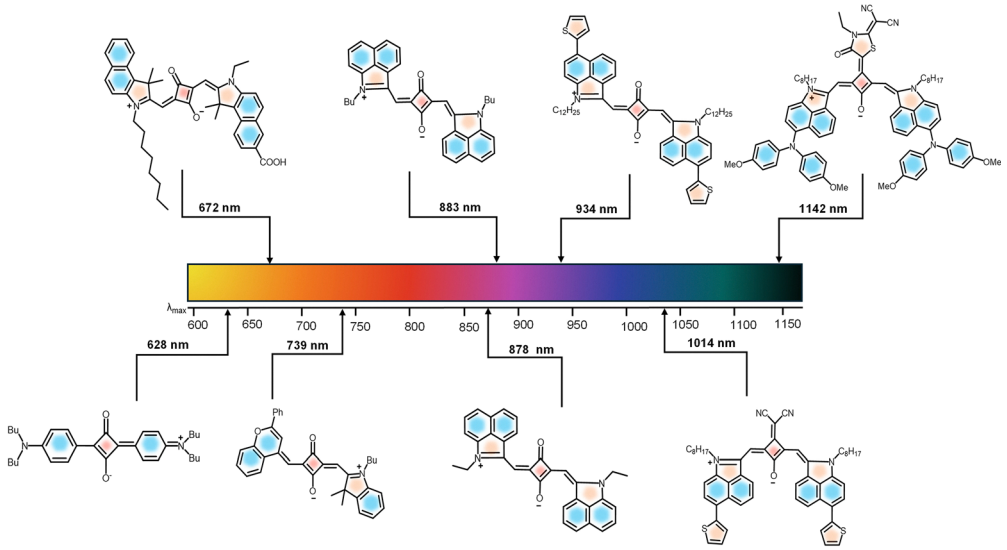

Fig. 3 Evolution of tunable optical properties in **SQ** derivatives from NIR-I to NIR-II and further. References for **SQ**s with absorption maximum at: 628 nm (ref. 3), 672 nm (ref. 10), 739 nm (ref. 3), 883 nm (ref. 3), 878 nm (ref. 42), 934 nm (ref. 42), 1014 nm (ref. 28) and 1142 nm (ref. 28).

sources. This photostability is attributed to the structural characteristics of squaraines, which include a cyclic framework that enhances their resistance to photodegradation. The combination of high molar absorptivity and photostability makes squaraine dyes particularly advantageous for applications in advanced optical imaging techniques such as photoacoustic imaging.[87,88]

Excited-state properties of squaraines

Detailed understanding of the excited-state properties of squaraine dyes is essential for their use in theranostic applications. Key parameters include fluorescence quantum yield, singlet oxygen generation,[89] and excited-state lifetime.[6] Squaraine dyes typically exhibit high fluorescence quantum yields, often exceeding 0.5, which indicates efficient radiative decay of the excited state. This high quantum yield is advantageous for applications requiring bright fluorescence, such as bioimaging and sensing. More importantly, squaraine dyes are known for their ability to generate singlet oxygen upon excitation, a property that is particularly relevant in photodynamic therapy (PDT).[90,91] The generation of singlet oxygen can lead to oxidative stress in targeted cells,[92] making squaraine dyes effective agents for cancer treatment.[93] The efficiency of singlet oxygen production is influenced by the dye's structure and the surrounding environment, with modifications to the dye, such as introducing electron withdrawing heavy atoms in the backbone, often enhancing its photodynamic efficacy.[94] The excited-state lifetime of squaraine dyes is another critical property, typically ranging from nanoseconds to microseconds, depending on the specific dye and its environment. Longer excited-state lifetimes can facilitate energy transfer processes and improve the efficiency of applications such as two-photon fluorescence imaging.[95] Understanding these excited-state dynamics is

crucial for optimizing the design of squaraine dyes for specific biphotonic applications.[96]

Chemical response mechanisms

The photophysical properties of squaraine dyes can be altered by external agents through changes induced in the intramolecular charge transfer (ICT) within the dye framework.[97] Factors such as solvent polarity, pH, and biomolecular interactions can influence the absorption and emission characteristics of these dyes.[98] The intense ICT within the donor–acceptor–donor (D–A–D) framework is highly dependent on the dipole moment of the dye in its ground and excited states. For instance, the introduction of *N,N*-dialkylaniline substituents enhances the sensitivity to solvent polarity. In polar environments the stabilization of the excited state leads to a pronounced spectral shift in both absorption and emission of the dyes.[99,100] This property can be exploited for sensing applications, where the dye's response to specific environmental changes can provide valuable information. Similarly, pH sensitivity is another important aspect of squaraine dyes.[101,102] Structural modifications such as incorporation of phenolic hydroxyl groups or tertiary amines on the aryl rings induce pH dependent changes. Protonation or deprotonation of these auxo chromic groups alters the electron donating strength of the D-groups, leading to changes in ground state and excited state properties of the dyes. The pH sensitivity can be utilized in biosensing applications, where the detection of pH changes in cellular environments is crucial for monitoring physiological processes.[103] Squaraine dyes often interact with proteins or nucleic acid through non-covalent interactions, including π–π stacking and hydrophobic interactions. Binding to the hydrophobic pockets of proteins such as albumin induces rotational restrictions and local microenvironmental polarity dependent changes in the photophysical properties of the dyes.[104,105] These interactions can be harnessed for developing biosensors and imaging probes that respond to specific biological targets.

Why choose squaraine dyes for biophotonic applications?

Squaraine dyes possess distinct advantages over traditional organic dyes and fluorescent proteins especially in biological applications, owing to their unique structural and photophysical properties.

(i) Higher photostability: one of the most notable advantages of squaraine dyes is their exceptional photostability compared to traditional organic dyes.[106] Many organic dyes are prone to rapid photobleaching, limiting their use in long-term imaging and sensing applications.[107] In contrast, squaraine dyes demonstrate remarkable resistance to photodegradation, enabling extended observation periods without significant signal loss.[108] This property is particularly beneficial for live-cell imaging and real-time sensing applications.

(ii) Narrow and intense absorption bands: squaraine dyes possess narrow and intense absorption bands in the near-infrared region, which is advantageous for minimizing background fluorescence and enhancing signal-to-noise ratios in sensing applications.[65] This feature allows for the detection of analytes at low concentrations, making squaraine dyes suitable for applications requiring high sensitivity.

(iii) Versatility in functionalization: the chemical structure of squaraine dyes allows for versatile functionalization, enabling the incorporation of specific recognition elements for target analytes.[5] This flexibility facilitates the design of highly selective sensors tailored to detect a wide range of analytes, including ions, small molecules, and biomolecules.[5] In contrast, traditional fluorescent proteins often have limited modification capabilities, restricting their application scope.

(iv) Reduced interference in biological systems: the photophysical properties of squaraine dyes in the NIR-I and NIR-II windows minimize interference from biological components, making them ideal for *in vivo* applications.[109] This feature ensures vivid imaging and sensing, resulting in complex biological environments,[110] where other dyes may suffer from autofluorescence or scattering.[111,112]

Consequently, squaraine derivatives are emerging as a promising alternative for traditional biophotonic probes. The excellent blend of photophysical behaviour and structural adaptability of squaraine dyes distinguishes them from other dyes such as indocyanine green (ICG),[113,114] cyanine (Cy5),[115,116] phthalocyanine,[117,118] BODIPY,[119,120] curcumin,[121,122] IR-1061-PEG nanoparticles,[123] SPN1,[124] SCH1100,[125] FD-1080,[126] CH1055,[127] IR-E1,[128] IR-FEP,[129] IR-FEPC,[130] IR-FG,[131] and IR-FTAP[132] dyes. A table comparing the photophysical properties of squaraine dyes with those of other dyes for biophotonics applications is given in Table S1. Furthermore, the inherent chemical versatility of the squaraine dyes facilitates precise modifications to enhance aqueous solubility and enables targeted functionalization for diverse biophotonic applications.

Molecular sensing using squaraines

Mechanistic overview of biosensing and detection

In squaraine dyes, ICT plays a key role in modulating the photophysical characteristics, efficiently leading to intriguing near-IR properties.[133,134] The changes in the electronic charge distribution can affect the reactivities of these dyes towards various analytes. The D–π–A zwitterionic backbone of squaraines[135] undergoes changes in ground state and excited state properties with respect to the substituent effects and their electron donating or withdrawing strength. Biosensing and detection using squaraine dyes proceed through two major pathways: analytes may bind either to the electron withdrawing cyclobutene ring or to the binding site embedded aromatic system in conjugation. This will induce significant changes in the photophysical as well as electrochemical properties of the dye systems.

The interaction of squaraines with analytes could be signalled by monitoring the extent of fluorescence quenching.[136] The photoinduced electron transfer (PET)[137] process occurs when the electron acceptor molecule interacts with excited state of squaraine dyes (donor), facilitating the transfer of an electron.[138] This electron transfer disrupts the radiative decay pathway, leading to a significant reduction in fluorescence intensity.

For example, in the presence of specific metal ions, PET can be facilitated leading to quenching of fluorescence.[139] This mechanism is advantageous for the detection of ions and small molecules as it allows a rapid and sensitive measurement of target analytes.[140]

Förster Resonance Energy Transfer (FRET) is a crucial process in squaraine-based probes, enabling efficient energy transfer between molecules.[141,142] In this process, an excited donor molecule, such as a squaraine dye, transfers energy to an acceptor molecule through dipole–dipole interactions.[143] Far-red-squaraine dyes not only enhance sensitivity by reducing biological autofluorescence but also offer depth penetration and effective signalling of binding events in biosystems.[144] FRET based probes are particularly valuable in biosensing applications, where squaraines are paired with complementary fluorescent probes.[143] Similarly, synergistic combination of aggregation induced quenching (AIQ) of fluorescence and the FRET process in squaraines could be another approach to facilitate biosensing applications.[145]

Squaraine dyes play a significant role in the sensitive and selective detection of small biomolecules through fluorescence turn-on/off mechanisms. The self-assembly approach also enables the recognition of large biomolecules and biorelevant metal ions *via* aggregation–disaggregation processes and targeted interactions, widening its applications in live cell imaging and *in vivo* imaging. Furthermore, squaraine derivatives have reached a milestone in bioimaging, through multiphoton deep-tissue visualization, photoacoustic imaging, and multimodal approaches for enhanced resolution and tumor mapping. As theranostic agents, these dyes facilitate photodynamic therapy by generating reactive oxygen species to induce cancer cell death, photothermal therapy through efficient light-to-heat conversion for tumor ablation, and targeted drug delivery using nanoparticles and hydrogels for controlled release, thus showing potential in advancing medical diagnostics and imaging modalities in medical applications.

Sensing of small biomolecules

Squaraine dyes have been widely used for the detection of biorelevant molecules such as phosphates, thiols, *etc.*[146] Selective detection of adenosine triphosphate (ATP) is made possible by a self-assembled ternary system *via* a signal turn-on approach. A cationic surfactant (cetyl trimethyl ammonium bromide (CTAB)) with ATP and squaraine dye **SQ1** acts as the ternary system for recognition of ATP.[147,148] CTAB interacts with the negatively charged ATP and with **SQ1**, resulting in fluorescence turn-on (Fig. 4). Upon electrostatic interaction with ATP, the H-aggregate of **SQ1** changes to the *J*-aggregate (head-to-tail arrangement), resulting in a red shift. The electrostatic interaction and π–π stacking of the aromatic segment of ATP and **SQ1** facilitates the selective detection of ATP.[148] Dicyanovinyl squaraine **SQ2** with a boronic acid group is a suitable probe for the fluorescence imaging of ATP in the NIR window. The phenylboronic acid group and an electron withdrawing cyano group improve the photostability of the dye. **SQ2** undergoes supramolecular self-assembly, upon addition of CTAB. Multiple electrostatic interactions between **SQ2**, ATP and CTAB molecules take place, causing fluorescence "turn-on" of **SQ2** with the maximum emission at 700 nm (Fig. 5). The probe showed excellent sensitivity and selectivity towards intracellular ATP in MCF-7 cells.[147]

An interesting set of self-assemblies based on DPA–Zn(II) derivatives (DPA-12@Zn(II) and DPA-16@Zn(II)) with a hydrophobic squaraine dye **SQ1** facilitate sensing of ATP with high selectivity in the NIR region.[149] DPA–Zn(II) derivatives serve as micelles to encapsulate the hydrophobic **SQ1**. In the presence of ATP, the phosphate anion is attracted by DPA–Zn(II) of the **SQ1**-embedded micelles *via* the metal–anion coordination interaction. At the same time, ATP can also undergo interaction with SQ located on the surface of micelles through electrostatic and π–π interactions. This self-assembly enables various biological applications such as ATP imaging in the gastric cancer cell line SGC-7901, selective detection of ATP in living cells and for monitoring its level fluctuation during the mitotic period.[149]

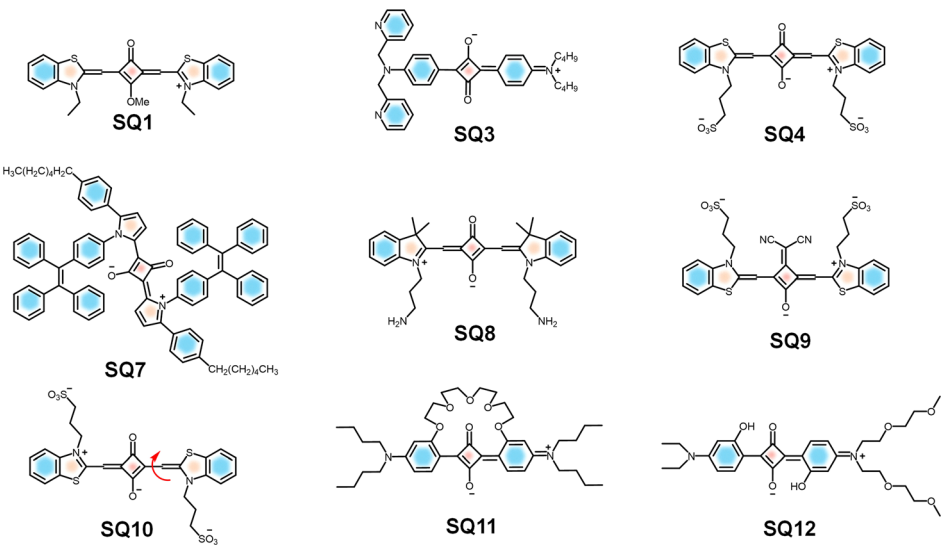

Fig. 4 Chemical structures of **SQ1**, **3**, **4**, and **7–12**.

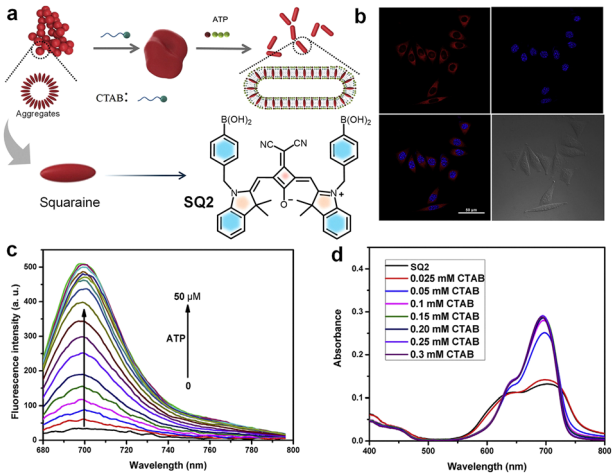

Fig. 5 (a) Illustration of self-assembly of **SQ2** in aqueous media and the detection mechanism. (b) Fluorescence images of MCF-7 cells incubated with **SQ2** for 2 h. (c) Emission changes of **SQ1** with the addition of ATP in PBS solution. (d) Changes in the absorption spectra of **SQ2** in PBS solution with increase in concentration of CTAB. Reproduced from ref. 147 with permission from Elsevier, Copyright 2019.

An unsymmetrical squaraine dye **SQ3**, which undergoes complexation with Zn^{2+} to form the **SQ3**–Zn^{2+} composite, distinguishes cyclic and linear phosphates.[150] **SQ3**–Zn^{2+} shows a blue shift compared to **SQ3**, due to quenching of the intramolecular charge transfer (ICT) band of the dye. The recovery of fluorescence from the complex occurs when another competing ligand attacks the Zn^{2+} centre. Zn^{2+} can bind well with ligands having nitrogen and oxygen, making it suitable for the detection of phosphates, particularly in nucleotides. Cyclic phosphates, such as cyclic adenosine monophosphate (c-AMP) and cyclic guanosine monophosphate (c-GMP), upon interaction with **SQ3**–Zn^{2+} showed a distinct absorption change, when compared to their linear counterparts. The linear phosphates, including pyrophosphate (PPi), caused a fluorescence turn-on at 659 nm that matches with the emission maximum of the parent dye (**SQ3**). Whereas, addition of cyclic analogues also caused a fluorescence turn on, however, with a 15 nm blue-shift of the maximum at 644 nm, which can be observed by the ''naked eye''. Thus, accessibility of the Zn^{2+} centre to monitor the fluorescence responses with the various nucleotides in biological systems is established.[150]

Similarly, another newly introduced squaraine system (**SQ4**) proved its ability to detect pyrophosphate (PPi) and alkaline phosphatase (ALP) by modulating the fluorescence of the dye.[151] The interaction of Cu^{2+} with **SQ4** forms a Cu^{2+}–**SQ4** system with significant quenching of fluorescence intensity. In the presence of PPi, the binding strength of Cu^{2+} towards PPi will be greater than that of Cu^{2+} towards **SQ4**. Consequently, the enhanced fluorescence intensity of the reaction system, comprising probe **SQ4** and Cu^{2+} facilitates the detection of PPi. The attack of ALP on the PPi–Cu^{2+} complex hydrolyses PPi, releases Cu^{2+} from the complex, and then Cu^{2+} reacts with **SQ4**, resulting in fluorescence quenching. Based on this ''off–on–off'' fluorescence response, the detection of PPi and ALP is made possible.[151]

In 2008, a weakly fluorescent NIR squaraine dye (**SQ5**) was reported by us for the estimation of low molecular weight amino thiols in human blood plasma (HBP). Thiol-containing amino acids such as cysteine (Cys) and homocysteine (Hcy) could be estimated using the **SQ5** probe.[152] **SQ5** is a weak fluorophore in its initial state, exhibiting weak NIR emission at 750 nm. **SQ5** having an extended π-conjugation results in notable absorption and emission changes in the presence of aliphatic thiols (Fig. 6). The nucleophilic attack by a thiol leads

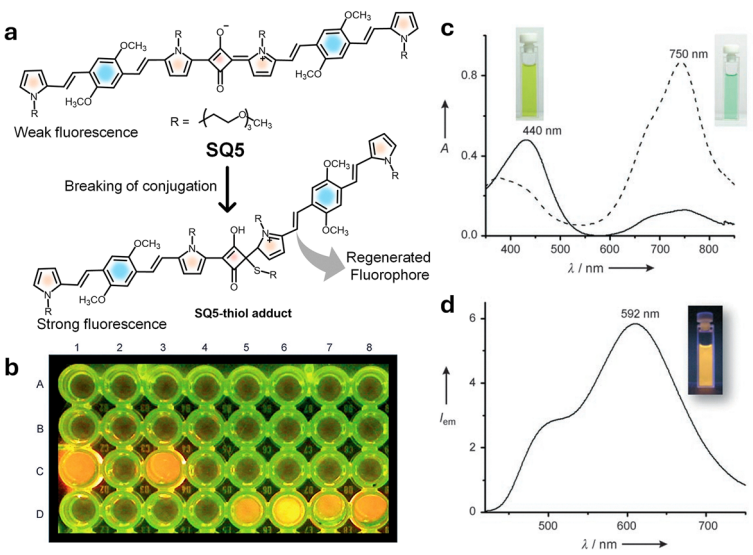

Fig. 6 (a) Mechanism of chemical activation of a weak fluorophore in **SQ5** using nucleophilic thiol attack. (b) Microwell test assay demonstrating detection of thiol containing aminothiols using **SQ5** (well A1), C1 L-cysteine (C1) and (glutathione) (C3), and different aliquots of human blood plasma samples after reduction (D5-D8). (c) UV-vis spectra of **SQ5** before and after addition of cysteine. (d) Emission spectrum of **SQ5**–thiol adducts and a photograph showing the corresponding fluorescence. Reproduced from ref. 152 with permission from Wiley VCH, Copyright 2008.

to the breaking of the π-conjugation, thereby modulating the fluorescence of **SQ5**. Therefore, upon addition of cysteine, a new strongly fluorescent species, the **SQ5**–cysteine adduct, is formed, with a new emission band at 420 nm when excited at 410 nm. This observation indicates that the fluorescence of **SQ5** is quenched in its dormant state, and thiol conjugation activates strong fluorescence. This system has been used to estimate the aminothiol concentration in blood before and after breakfast, and after smoking, to study the effect of food intake and smoking on the variation of blood aminothiols. The probe can have further applications in the fluorescence labelling and imaging of thiol containing proteins in biological fluids.[152]

An unsymmetrical NIR active squaraine probe **SQ6** was reported for aminothiol detection, using NIR fluorescence and multispectral optoacoustic tomography (MSOT) signal responses.[153] Dye **SQ6** displayed a narrow and intense absorption-emission peak in the range of 680 to 705 nm.[63] **SQ6** upon reacting with aminothiols (glutathione, GSH) formed the **SQ6**–GSH adduct with a decreased absorption maximum at 670 nm, accompanied by the formation of a new band at 380 nm (Fig. 7). Simultaneously, quenching of the 700 nm emission occurred and displayed a new band at 520 nm, resulting in the activation of strong fluorescence. The response of **SQ6** to biological thiols was evaluated in the human hepatoma cell line (Huh-7 cell line). Fluorescence microscopy under 405 nm excitation showed strong green fluorescence, confirming **SQ6** internalization and conjugation with cellular thiols, while 620 nm excitation produced weak red fluorescence.[153]

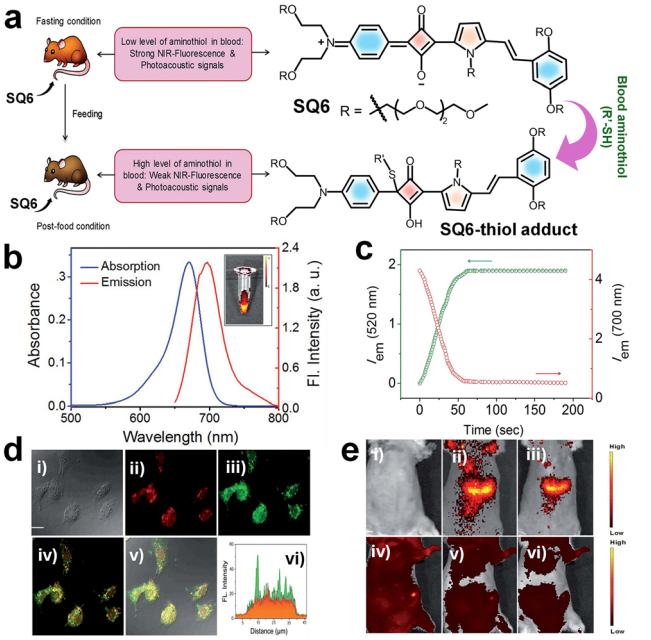

Fig. 7 (a) Schematic representation of fluorescence and photoacoustic bimodal signaling for *in vivo* detection of aminothiol content using **SQ6**. (b) UV/vis-absorption (blue curve) and emission spectra (red curve) of **SQ6**. (c) Fluorescence intensity changes at 520 nm (λ_{ex} = 380 nm) and 700 nm (λ_{ex} = 640 nm) produced by the reaction of **SQ6**, monitored at 1 s intervals. (d) Fluorescence microscopy images of Huh-7 cells incubated with **SQ6** for 12 h (scale bar = 1.5 mm). (e) *In vivo* fluorescence reflectance images obtained after injecting with **SQ6** in fasting mouse (i–iii) and post-food mouse (iv–vi). Reproduced from ref. 153 with permission from The Royal Society of Chemistry, Copyright 2016.

An *in vivo* imaging study on seven-week-old female severe combined immune deficiency (SCID) mice was performed to evaluate the performance of **SQ6** in detecting aminothiols using fluorescence and photoacoustic imaging techniques (a bimodal approach). Fluorescence imaging was performed on fasting mice, followed by photoacoustic imaging after administering **SQ6** (2 mM, 200 μL). Strong red fluorescence appeared at 15- and 40-minutes post-injection, indicating **SQ6** distribution in the bloodstream and abdominal region. After feeding, fluorescence signals weakened, suggesting increased concentration of thiol, which reacts with **SQ6**. Photoacoustic imaging confirmed abdominal accumulation and revealed higher aminothiol levels post-feeding through a spectral unmixing approach. This dual imaging strategy shows promise for non-invasive detection of aminothiols, potentially aiding early diagnosis of diseases such as coronary heart disease.[153] In a related study involving **SQ6** (Fig. 8), the dye was found to undergo self-assembly to form a nonfluorescent nanoparticle (NP).[63] Remarkably, this NP exhibited a selective response to human serum albumin (HSA), generating a distinct green emission even in the presence of other thiol-containing molecules and proteins. This selective actuation enables reliable detection of HSA in blood serum. Moreover, **SQ6** alone showed non-selectivity and failed to respond to any thiol-containing proteins and small molecules, underscoring the functional advantage of its nanoparticle form.[63]

Another approach was to use aggregation-induced emission (AIE)[154] of squaraines as a tool for the detection of thiol-containing biomolecules, such as cysteine (Cys) and glutathione (GSH).[155] For this purpose, AIE-active triphenylethylenyl and tetraphenylethylene (TPE) moieties functionalized at the 2- and *N*-positions of the pyrrole unit, respectively, were condensed with squaraines to get dye **SQ7** (Fig. 4). Upon the interaction of a nucleophile with the squaraine core, N-TPE exhibited AIE properties. Selectivity studies confirmed that AIE active dyes selectively respond to biologically active thiols, Cys and GSH.[155]

Recently, the detection of carbonic anhydrases (CAs) in whole blood is made possible by a disassembly-driven squaraine based fluorescent nanoprobe (**SQ8**).[156] Carbonic anhydrases (CAs) are zinc-containing metalloenzymes and are critical biomarkers in cancer diagnosis and therapy. The nanoprobe exhibits small-molecule self-assembly, forming stable and well-ordered aggregates with minimal background fluorescence. Since the absorption spectrum of the probe (around 600 nm) overlaps with blood autofluorescence, it suppresses autofluorescence of the blood through an inner filter effect. CAs upon binding to the probe facilitate disassembly of the probe and eliminate aggregation caused quenching (ACQ), thereby restoring fluorescence. These synergistic mechanisms result in a fluorescence enhancement of approximately 45-fold upon interaction with 3 μM CA IX, significantly improving the detection sensitivity and specificity. Nanoprobe **SQ8** enables quantification of endogenous CAs in human blood and detection of elevated CA levels in untreated lung cancer patients and tracked therapeutic response, underscoring its diagnostic utility.[156]

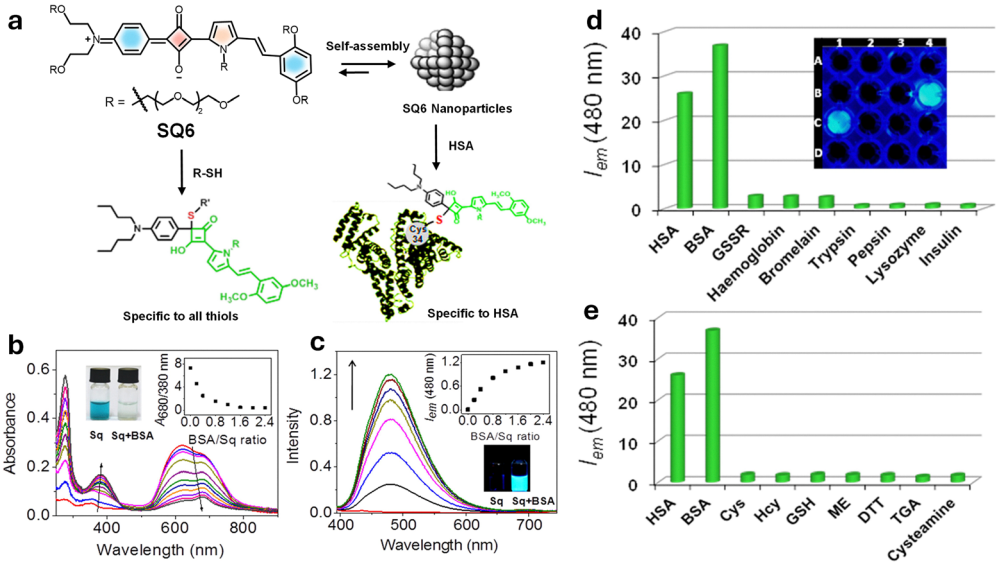

Fig. 8 (a) Schematic representation of **SQ6** dye nanoparticles designed for the specific sensing of serum albumin proteins. (b) UV-vis absorption spectrum of **SQ6**; (c) fluorescence intensity changes upon addition of BSA; (d) and (e) fluorescence response of SQ nanoparticles at 480 nm monitored against 1 equivalent of HSA and BSA and 10 equivalents of various other proteins and small molecules. Reproduced from ref. 63 with permission from American Chemical Society, Copyright 2014.

Large biomolecule detection

G-quadruplexes[157] are four-stranded nucleic acid structures formed by guanine-rich sequences that play key roles in genomic stability, gene regulation, and potential therapeutic targeting. The development of squaraine probes for G-quadruplex (G4) recognition in biological samples requires precise structural design of the dyes.[158] Squaraine dye **SQ9** (Fig. 4) exhibits strong interaction with the parallel G4s, but no interaction with other DNA forms. Upon addition of parallel G4s (EAD, Pu22, c-kit2, and c-kit87up), the absorption spectra of **SQ9** showed an increase in monomer band and decrease in H-aggregate band with increasing concentration of EAD. **SQ9** was present as H-aggregates in aqueous medium, whereas **SQ10** (Fig. 4) was present as both H-aggregates and monomers. The addition of parallel G4s caused the transformation of **SQ9** from aggregates to monomers, but did not cause significant transformation of **SQ9**. The fluorescent spectra indicated that parallel G4s could enhance the fluorescence of both **SQ10** and **SQ9**, but the fluorescence enhancement of **SQ9** was higher than that of **SQ10**, indicating the higher affinity of **SQ9** to parallel G4s. The dicyanomethylene substitution in **SQ9** gives it a cisoid conformation; this V-shaped conformation was considered to contribute to the high selectivity of **SQ9** to parallel G4s. The excellent selectivity to parallel G4s and the favourable optical properties of squaraine dye allow **SQ9** to serve as a ''light-up'' fluorescent probe to distinguish parallel G4s from other DNA forms in biological samples.[158]

The squaraine derivative **SQ11** was designed for the detection of human serum albumin (HSA) in blood. In aqueous environments, it forms nano-aggregates driven by hydrophobic interactions exhibiting a weak absorption band at 660 nm.[159] Due to the induced aggregation of **SQ11**, the fluorescence signal undergoes a ''turn-off'' process and the subsequent ''turn-on'' response upon interaction with HSA facilitates effective protein–ligand recognition. The fluorescence intensity of **SQ11** at 675 nm increased dramatically with 20-fold enhancement with increasing concentration of HSA to 25 μM due to the disaggregation of **SQ11** nanoparticles. This disaggregation-based mechanism is particularly promising for cell imaging. *In vitro* fluorescence imaging studies were performed using the **SQ11**–HSA complex in HeLa cancer cells. Furthermore, HeLa cells treated with the **SQ11**–HSA complex for 1 h emit bright red fluorescence, with distribution inside the cytoplasm as well as on the cell surface. Due to the high selectivity and low detection limit of HSA, this sensing mechanism could be applied widely in near infrared fluorescence detection of biological proteins.[159]

Owing to its high structural similarity with HSA, bovine serum albumin (BSA) has been investigated as a model protein in different fields. A squaraine-based fluorescent molecule, **SQ12** (Fig. 4), was designed for the selective detection of BSA.[160] **SQ12** is non-fluorescent in aqueous solution due to the aggregation caused quenching (ACQ) effect. Upon addition of BSA, the fluorescence intensity at 664 nm was gradually increased, indicating a ''turn-on'' response due to disaggregation upon binding. When 0.3 mM BSA was added, about a 10-fold increase in fluorescence intensity was observed. The fluorescence response of **SQ12** to other proteins and enzymes, amino acids, ATP, and DNA revealed that interaction between BSA and **SQ12** results in a significant increase of fluorescence, whereas others did not show any change. This effective and selective interaction with BSA opened a pathway for the *in vitro* fluorescence imaging studies. *In vitro* studies in HeLa cells confirm its potential for bioimaging, positioning it as a versatile platform for biological and diagnostic applications.[160]

Highlighting the application of squaraine dyes for labelling of oligonucleotides, a dye with fluorinated benzothiazole rings (**SQ13**) (Fig. 9) was designed.[161] The selective detection of specific DNA and RNA sequences can be achieved by using oligonucleotide probes complementary to the target sequence and containing a reporter group and by using fluorescence spectroscopy for monitoring. For labelling oligonucleotides with **SQ13** a post-synthetic coupling strategy is used. One of the benzothiazole rings is methylated and the other is alkylated with a diiodohexyl linker in order to react the squaraines with a thiophosphate group incorporated at the 5′-position of the oligonucleotides, forming a phosphor thiol diester linkage. The oligonucleotides labelled with the squaraines exhibited high fluorescence emission. It was observed that fluorination of the benzothiazole moiety of the squaraine led to an improvement in photostability and chemical stability. Thus, fluorinated squaraine dyes are considered as promising tools for the labelling of oligonucleotides.[161]

Similarly, an oligo (ethylene glycol)-functionalized squaraine fluorophore (**SQ14**-Leu) has been reported as a NIR-fluorescent probe to detect and image the activities of a diagnostic enzyme, leucine aminopeptidase (LAP), both *in vitro* and *in vivo*.[162] **SQ14**-Leu showed near-infrared absorption and emission with a low detection limit (0.61 ng mL^{-1}), good aqueous solubility, low toxicity, high selectivity and sensitivity toward LAP. *In vitro* imaging of HepG2 cells, LO2 cells, and L929 cells was performed by incubating them with the **SQ14**-Leu solution under controlled conditions before and after the addition of the dye. The **SQ14**-Leu probe enabled fluorescence sensing of LAP in cells, which confirmed that the probe could serve as a detection system for tracking LAP *in vitro*. The probe could be used for *in vivo* imaging of HepG2 xenograft tumours in a mouse model.[162]

Neutrophil extracellular traps (NETs) are web-like structures released by neutrophils, a type of white blood cell, to capture and destroy pathogens like bacteria, fungi, and parasites.[163] NETs are composed of condensed DNA, histones, neutrophil elastase (NE), cathepsin G, myeloperoxidase (MPO), *etc*.[164] Squaraine dye-peptide conjugates (**SQ15**-NETP) enable the detection of NETs. **SQ15**-NETP, a NIR fluorescent probe, undergoes self-quenching, leveraging the protease activity of neutrophil elastase (NE), for the real-time detection and imaging of NETs. The probe covalently binds to NE, resulting in high resolution imaging and stability in *ex vivo* samples (Fig. 10). The air pouch model was used to investigate NET formation induced by monosodium urate (MSU) crystals in mice, using *in vivo* imaging. Injection of MSU triggers an inflammatory response characterized by neutrophil infiltration into the air pouch leading to the formation of NETs. This model also facilitates the pouch fluid to be collected for the subsequent NET analysis. Moreover, high specificity and biocompatibility of the probes make them promising tools for diagnostic and therapeutic strategies in managing inflammatory diseases and cancers.[163]

Sensing of biorelevant metal ions

A careful design approach by the introduction of metal ion chelating moieties in the donor–acceptor backbone of squaraines results in a class of sensors specific for different metal cations. Modulation of aggregation behaviour of squaraines in the presence of metal ions results in probes capable of sensitive and selective detection of ions, often visible by the naked eye. Notably, Ca^{2+} sensors gained attention, as they exploit the principle of a metal-ion induced conformational folding of a rigid-flexible-rigid bichromophore to form an ''H'' foldamer, leading to significant variation in optical properties due to the exciton interaction.[165,166] A rigid–flexible–rigid bichromophore

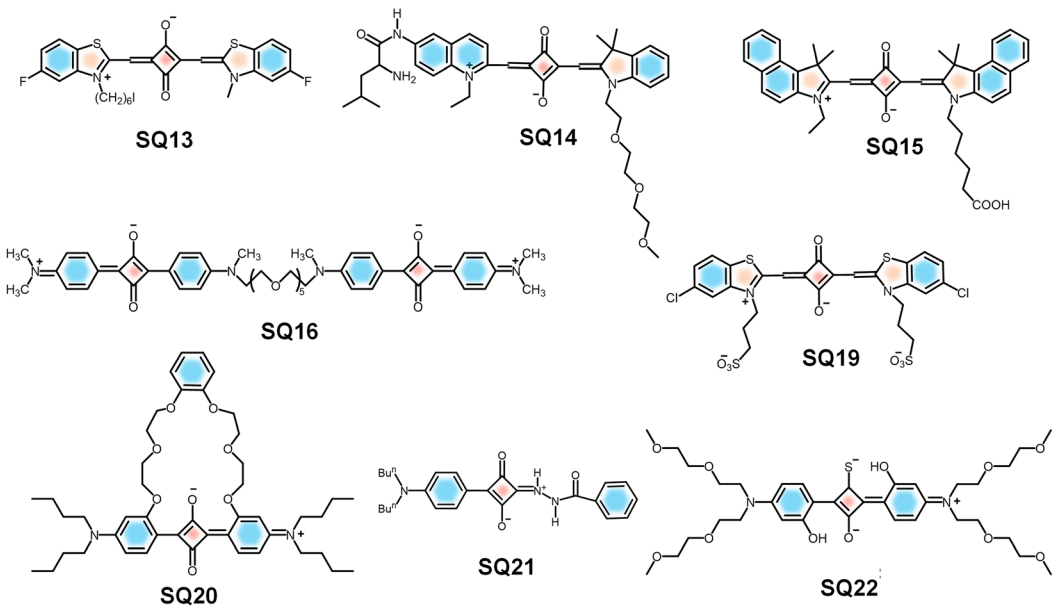

Fig. 9 Molecular structures of SQs reported for oligonucleotide labelling (**SQ13**), detection of LAP (**SQ14**), detection of NETs (**SQ15**), and biorelevant metal ions (**SQ16, 19–22**).

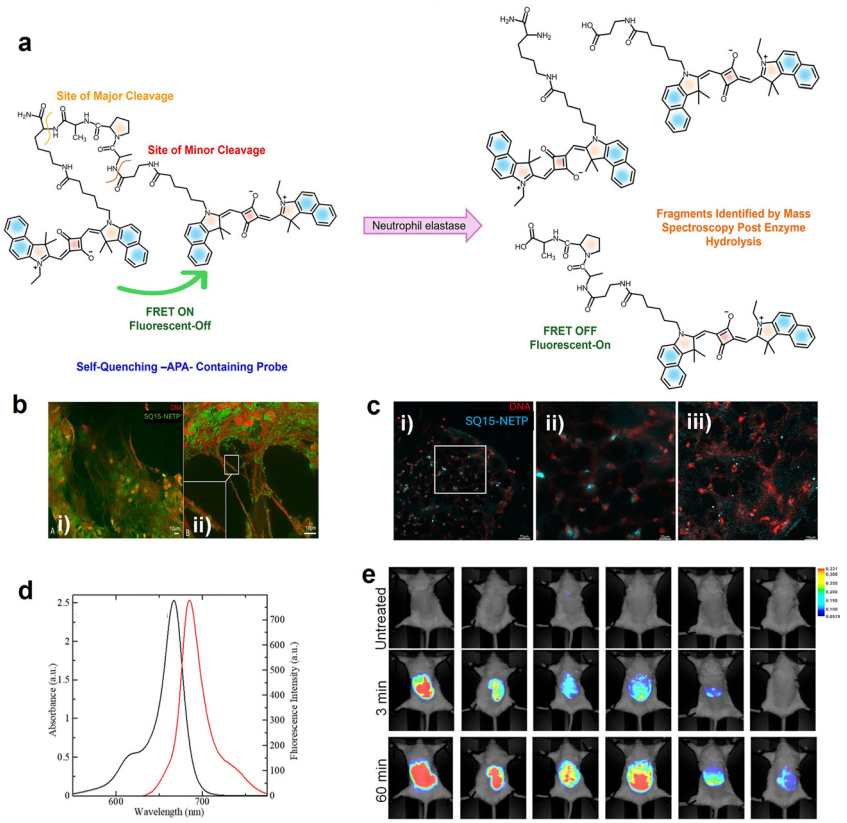

Fig. 10 (a) Schematic representation of the mechanism behind the reactivation of fluorescence of **SQ15** in the presence of neutrophil elastase (NE). (b) Evaluation of **SQ15**-NETP localization in human neutrophil extracellular traps (NETs) from a mucosal surface using (i) fluorescence microscopy and (ii) fluorescence imaging integrated with optical sectioning techniques. (c) Fluorescence imaging of human coronary thrombi; (i) wide field scan showing NETs within thrombi treated with 800 nM **SQ15**-NETP; (ii) magnified view of the selected region from (i) with enhanced depth of field; (iii) confocal scan of the same area confirming that the previously blurred signals correspond to specific NE-positive granules of DNA fibers. (d) Absorption (black) and emission (red) spectra of **SQ15** (10 μM) in $CHCl_3$. (e) *In vivo* comparison of FRET-based probes in the air pouch with MSU-induced NETs. Reproduced from ref. 163 with permission from American Chemical Society, Copyright 2025.

system composed of a squaraine core (**SQ16**) (Fig. 9) serves as the signalling unit and an oxyethylene chain serves as the flexible recognition moiety. The interaction of metal ions such as K^+, Na^+, and Mg^{2+} with a rigid–flexible–rigid bichromophore did not alter its absorption and emission properties. Whereas, upon binding with Ca^{2+}, it showed a visible colour change from intense blue to intense purple-blue, due to the hypsochromic shift of the absorption maximum from 630 nm to 552 nm. This observation indicates the selectivity of the rigid–flexible–rigid bichromophore toward Ca^{2+}.[165,166] However, the lack of water solubility of foldamer systems and formation of aggregates under aqueous conditions limit their applications in biological systems.

Cu^{2+} plays a pivotal role in many fundamental physiological processes. For example, Cu^{2+} in the cells will affect the enzyme activity and inhibit normal metabolism of cells and an excess amount could cause serious diseases, like gastrointestinal disturbance and liver or kidney damage.[167,168] The soft transition metal ion (Cu^{2+}) specific recognition[169] was achieved using squaraine based chemosensors **SQ17** and **SQ18** that are functionalized with 2-picolyl units[170] (Fig. 11). Cu^{2+} quenches nearly 85 percent of the fluorescence intensity of **SQ17** in the presence of the same amount of various metal ions. Similarly, upon addition of 1.0 equivalent of Cu^{2+} to a solution of **SQ18**, the bright purple color turns blue-black. Therefore, these two probes can enable "naked-eye" detection of Cu^{2+} in the visible wavelength region. The high selectivity of **SQ18** to Cu^{2+} clearly established that **SQ18** had the potential application of serving as a fluorescent probe for live-cell imaging, thus revealing the role of Cu^{2+} in biological systems under either *in vitro* or *in vivo* conditions.[170]

Similarly, H-aggregates of a squaraine dye (**SQ19**) can be utilized to detect Cu^{2+} in solvents. Addition of 5 mmol L^{-1} Ca^{2+} to **SQ19** forms H-aggregates of **SQ19**.[52] Further addition of Cu^{2+} leads to disassembly of H-aggregates into their monomers, leading to a color change from pink to blue, allowing the "naked-eye" detection of Cu^{2+}. H-aggregates did not dissociate to monomers with other metal ions, indicating the selectivity of the probe towards Cu^{2+}. Moreover, water solubility and biocompatibility of the probe make it a suitable tool to detect exogenous Ca^{2+}/Cu^{2+} in living cells.[52] **SQ20** is a polyether bridged squaraine dye (Fig. 9) having absorption in the near-infrared (NIR) region (642–650 nm) and was developed for the selective detection of Pb^{2+}.[171] This probe showed a specific "turn on" fluorescence

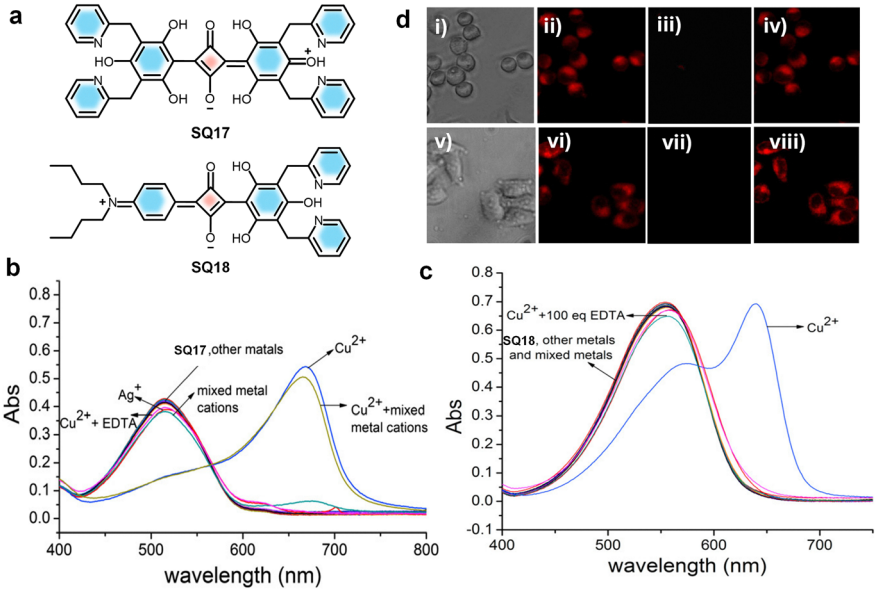

Fig. 11 (a) Chemical structures of squaraine dyes **SQ17** and **SQ18**. (b) and (c) UV-vis absorption changes of **SQ17** and **SQ18**, respectively, upon addition of 1 equivalent of various chloride salts. (d) Brightfield and fluorescence images of LL/2 (i–iv) and HepG2 (v–viii) cells. Brightfield and fluorescence images of LL/2 (i–iv) and HepG2 cells (v–viii); (i, v) bright field images of LL/2 and HepG2 cells; (ii, vi) fluorescence images following staining with 20 mM **SQ18** at 37 °C for 1 h (LL/2) and 0.5 h (HepG2), respectively; (iii, vii) fluorescence response after supplementation with $CuCl_2$ (100 mM); (iv, viii) restoration of fluorescence after addition of EDTA. Reproduced with permission from ref. 170, Elsevier, Copyright 2019.

response to Pb^{2+} with a detection limit of 1.70×10^{-8} M, which allowed identification of Pb^{2+} in the presence of other competing ions. Upon addition of Pb^{2+} to **SQ20**, a complex between Pb^{2+} and **SQ20** was formed, leading to the disaggregation of **SQ20** aggregates, resulting in the restoration of the emission of the **SQ20** monomer. ^{1}H NMR titration experiments and infrared spectroscopy proved chelation of Pb^{2+} with the ethylene oxide chain of **SQ20**. This novel fluorescent probe was used for the fast detection of Pb^{2+} in urine and dried shrimp samples.[171]

Maintaining optimal levels of Al^{3+} in the human body is crucial, as excess accumulation can lead to bone softening, bladder cancer, Parkinson's disease and Alzheimer's disease, and so on.[172–174] The fluorescent dye **SQ21** (Fig. 9) is an excellent probe for the selective and sensitive detection of Al^{3+}.[175] The benzylhydrazine moiety leverages the squaraine scaffold's strong absorption around 500 nm, along with oxygen and nitrogen donor sites favourable for Al^{3+}coordination. Upon Al^{3+} interaction with the probe, a "turn-on" mechanism occurs due to the photoinduced electron transfer (PET), enhanced intramolecular charge transfer (ICT), and chelation-enhanced fluorescence (CHEF). Biocompatibility of **SQ21** was confirmed *via* MTT assay on HUVEC cells, showing 102% cell viability at 10 μM after 24 h. In cell imaging, HUVEC cells incubated with 10 μM **SQ21** exhibited weak fluorescence, which significantly increased upon addition of 30 μM $Al(NO_3)_3$, with signals localized in the perinuclear region, indicating cell membrane permeability and suitability for intracellular Al^{3+} detection.[175]

Hg^{2+} ions have a high chance of bioaccumulation in living organisms, leading to severe health problems including central nervous system defects and erythrism as well as arrhythmias, cardiomyopathies, and kidney damage.[176,177] The monothiosquaraine dye (**SQ22**) (Fig. 9) exhibits near-infrared fluorescence, ultrahigh brightness, fast response, high sensitivity and excellent selectivity. Hence the dye is found to be suitable as a probe for the detection of Hg^{2+} ions as well.[178,179] **SQ22** has excellent selectivity and specificity for Hg^{2+} over other thiophilic metal ions such as Ag^+, Pb^{2+}, and Cd^{2+}. High sensitivity, an optimal pH range of 3–7, low detection limit, good water-solubility and low cytotoxicity of **SQ22** make it suitable for imaging Hg^{2+} in live cells and zebrafish. HeLa cells were treated with different concentrations (1–100 μM) of **SQ22** for 24 h. A weak fluorescence was observed when HeLa cells were treated only with **SQ22**, while ultrabright intracellular fluorescence from HeLa cells stained with Hg^{2+} was clearly observed. *In vivo* fluorescence imaging was done on five-year-old zebrafish, incubated for 20 min at 21 ± 1 °C in 4.0 μM **SQ22**, which revealed that the zebrafish showed negligible luminescence, but upon treatment with Hg^{2+}, an enhancement in luminescence was observed. Thus, the Hg^{2+} probe exhibited high selectivity against metal ions in biological systems.[178]

Bioimaging using squaraine derivatives

Several innovative bioimaging techniques have contributed to the advancement of biomedical research by providing a non-invasive approach to visualize specific biological activities with minimal interference with physiological processes.[180] Squaraine derived NIR dyes exhibit structural rigidity, tunable absorption wavelength, strong NIR absorption characteristics, and excellent photothermal stability under ambient conditions.[181] These

properties make them highly versatile for bioimaging applications, including fluorescence imaging, multiphoton imaging, and photoacoustic imaging.[182] The absorption and emission wavelengths of squaraines can be tuned across the visible to infrared spectrum, which enables their effective use in deep-tissue imaging applications. Moreover, they exhibit minimum autofluorescence, reduced light scattering, and enhanced signal-to-noise ratios.[183] Functionalization strategies, such as the incorporation of hydrophilic groups and encapsulation in nanoparticles or micelles, address challenges like aqueous solubility and aggregation, enhancing their biocompatibility and performance in complex biological environments.[184]

Near-infrared fluorescence imaging (NIRF)

Intense NIR emission of squaraine dyes enables visualization of cellular and tissue-level processes by NIR-fluorescence imaging, with high sensitivity and specificity.[185] The narrow absorption bands and high fluorescence quantum yields of these dyes facilitate detection at low concentrations, thereby reducing cytotoxicity and background fluorescence, which is critical for effective live-cell imaging.[186] Their photostability and low cytotoxicity make them suitable for *in vitro* and *in vivo* bioimaging.[187] Chemical structures of a selection of dyes with interesting properties are given in Fig. 12.

The ultrabright squaraine fluorophore **SQ23**, designed for near-infrared (NIR) fluorescence-guided surgery (FGS)[188–190] in epithelial ovarian cancer, addresses the crucial issue of identifying residual tumour post-surgery, which significantly influences the treatment outcome.[191] **SQ23** has favourable pharmacokinetic properties, featuring low serum binding and rapid tumor localization through organic cation transporters (OCTs), while its lysosomal retention enhances imaging stability for up to 24 h during operations. This innovative technique, along with the use of renal-clearable ZW800-PEG for imaging tumours and ureters, marks a noteworthy advancement in surgical oncology, potentially improving surgical resection, allowing real-time visualization of metastatic nodules.[191]

Similarly, squaraine based symmetrical and unsymmetrical probes have also been explored as the bioimaging materials. A water-soluble NIR-absorbing derivative, **SQ24**, was synthesized, using the indolizine derivatives as end groups. **SQ24** showed a very high Φ_{PLQY} of 58% with absorption and emission >700 nm in foetal bovine serum.[192] Upon comparison with the indocyanine green (ICG) dye, **SQ24** exhibited higher molecular brightness, prolonged photostability and low cytotoxicity, making it a suitable probe for NIR biological imaging.[192]

Consequently, squaraine-based conjugated polymers play a significant role in bioimaging, due to larger Stokes shifts and higher PLQYs in the NIR region.[193] A series of SQ-based, pH responsive NIR emitters with high photostability have been developed by covalently incorporating a squaraine into the polyfluorene backbone, namely **SQ25** (Fig. 12). When the concentration of the dye is less than 5% in the squaraine-based polymers, the fluorescence self-quenching was suppressed. **SQ25** can be used to detect even minute intracellular pH changes effectively in living MCF7 cells.[193]

As mentioned previously, the major drawback of squaraines includes their inherent reactivity with nucleophiles, leading to loss of the photophysical properties, and they have a high tendency to form nonfluorescent aggregates in aqueous medium.[194] Smith *et al.* have developed molecular systems by encapsulating the dye inside an amide-containing macrocycle.[59,195] Such rotaxanes

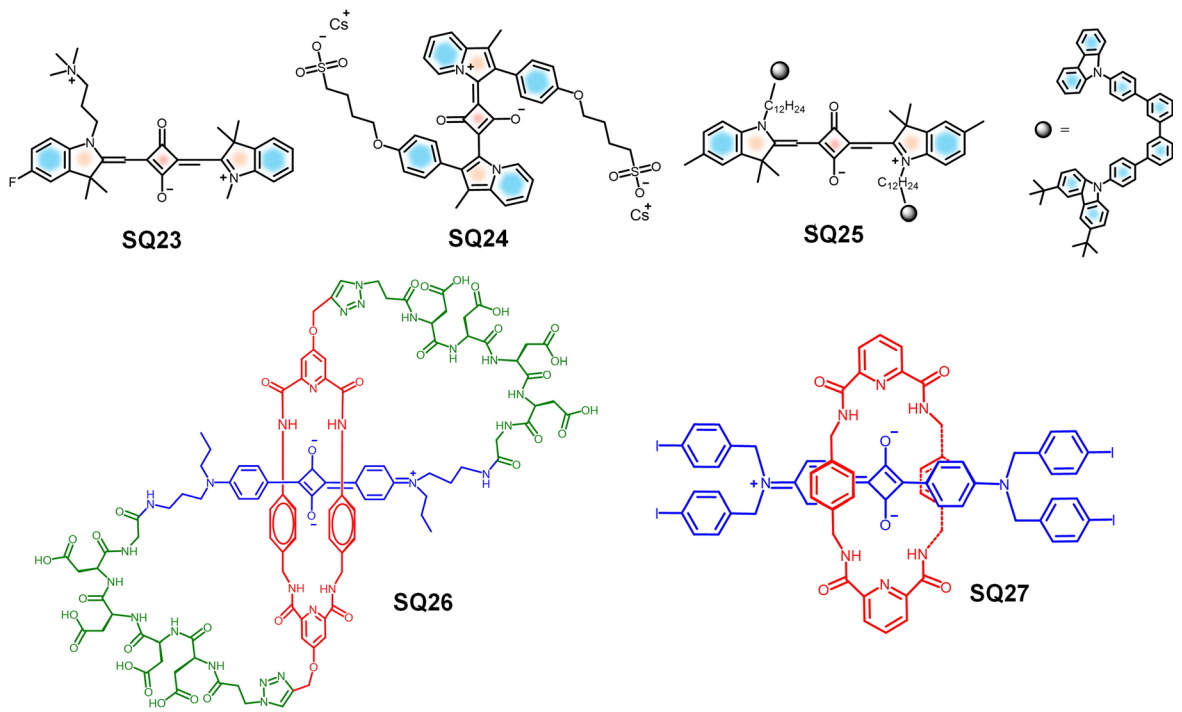

Fig. 12 Molecular structures of different **SQ** dyes reported for NIR imaging.

consist of one or more macrocyclic rings mechanically interlocked onto a stoppered axle.[196,197] A squaraine rotaxane was synthesized by a clipping approach, wherein a dumbbell-shaped squaraine moiety was used as a template to direct the formation of a Leigh-type amide-containing macrocycle, resulting in enhanced chemical stability of the squaraine dye.[58,198] Since it is straightforward to synthesize squaraines with unsymmetrical structures and as oligomers, it should be possible to prepare a wide range of squaraine-derived rotaxanes.[12,199] The squaraine-rotaxane macrostructures demonstrate exceptional resistance to both chemical and photochemical degradation and are useful as versatile fluorescent scaffolds for constructing various types of highly stable, near-IR imaging probes.[59,200] These NIR fluorescent probes hold significant biological relevance, particularly in applications such as *in vivo* imaging and theranostics.

Interestingly, the water-soluble dye **SQ26** (Fig. 12) is a deep-red fluorescent dye, having self-threaded molecular architecture that provides structural rigidity while simultaneously encapsulating and protecting the emissive fluorochrome. **SQ26** exhibits high stability, mainly due to the presence of the surrounding macrocyclic component, which sterically shields the encapsulated squaraine backbone and effectively prevents nucleophile attack. In addition to this, the constrained peptidyl loops resist the degradation of the dye by protease enzymes. While the polyanionic nature of **SQ26** limits cellular permeability, the presence of tetra-aspartate loops promotes selective binding to the mineral matrix within bone tissue. Thus, targeted fluorescence imaging of the bone in the complex biological environments, including histological sections and living animal models, is made possible.[201] In addition to these examples, a similar class of squaraine rotaxanes such as **SQ27** have also demonstrated therapeutic efficacy, which is discussed later in this paper.

The development of a new class of biologically relevant tetra lactam macrocycles capable of forming self-assembled complexes with squaraines in weakly polar solvents is an interesting progress in this direction. The dye encapsulation remains effective in highly competitive media such as mixed aqueous/organic solutions, vesicle membranes, and intracellular organelles. NIR imaging of live Chinese hamster ovary (CHO) cells was demonstrated using squaraine-rotaxane dye systems.[202] In a similar study, an unsymmetrical squaraine-rotaxane **SQ28Rot** dye was reported with mitochondrial localization capability, maintaining high stability and imaging performance within the organelle[203] (Fig. 13).

A new organic inorganic hybrid using **SQ29** was developed by loading the dye into mesoporous silica nanoparticles (MSNPs) and then wrapping the nanoparticle surfaces with ultrathin graphene oxide (GO) sheets by electrostatic interactions, resulting in the formation of GO–MSNPs[204] (Fig. 14). This process enables us to overcome the major limitations of squaraine dyes such as formation of aggregates in aqueous environments and vulnerability to nucleophilic attack. GO–MSNP1 shows remarkable stability, protecting the dye from degradation by thiols such as cysteine and glutathione while maintaining red-shifted absorption (595 nm) and emission (607 nm) in water with a quantum yield of 0.21. The hybrid showed low cytotoxicity in HeLa cells and enabled effective *in vitro* fluorescence imaging, with red emission observed in the cytoplasm and on cell surfaces. Therefore, the GO-wrapped system provides a biocompatible platform for protecting squaraine dyes, with biological applications such as targeted cellular imaging.[204]

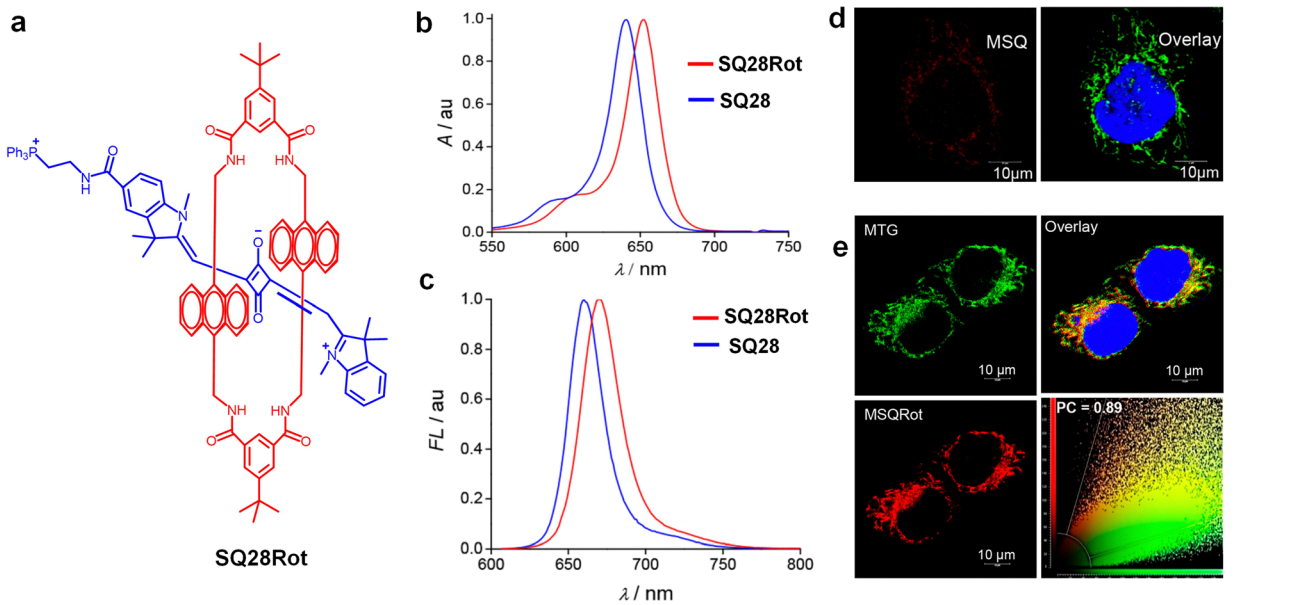

Fig. 13 (a) Chemical structure of a squaraine-rotaxane, **SQ28Rot**. (b) UV-vis absorption spectra of **SQ28Rot** in $CHCl_3$. (c) Fluorescence emission spectra of **SQ28Rot** in $CHCl_3$. (d) Confocal fluorescence images showing colocalization of **SQ28** with MitoTracker Green (MTG) in HeLa cells. (e) Confocal images of **SQ28Rot** colocalized with MTG in HeLa cells. Colocalization scatter plot indicates a Pearson coefficient of 0.89. Reproduced with permission from ref. 203, American Chemical Society, Copyright 2020.

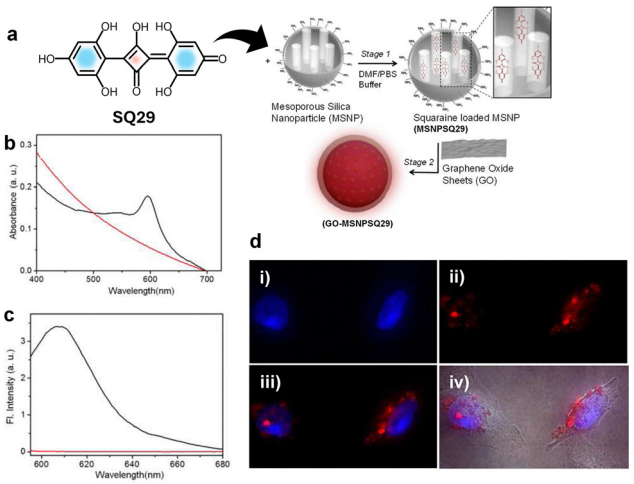

Fig. 14 (a) Structure of **SQ29** and its encapsulation within 3-aminopropyltriethoxysilane APTES-modified MSNPs followed by electrostatic wrapping of GO sheets onto the surfaces of **SQ29**-loaded MSNPs. (b) UV-vis absorption and (c) emission (λ_{ex} = 580 nm) spectra of GO−MSNPSQ29 (black) and GO−MSNP (red). (d) Epifluorescence microscopy images of HeLa cancer cells labeled with GO−MSNPSQ29, (i) image of nuclei. (ii) Fluorescencefluorescence of GO−MSNPSQ29 (dark-field). (iii) Overlay of (i) and (ii). (iv) Overlay of (iii) with the phase contrast image. Reproduced with permission from ref. 204, American Chemical Society, Copyright 2012.

In vivo imaging

Molecular probes for *in vivo* imaging applications are designed to visualize biological processes within living organisms with high specificity, minimal toxicity and strong signal to noise ratios. High photostability, deep tissue penetration capability, low background autofluorescence and compatibility with biological systems are the key requirements of a successful system.[65,205] Recent studies have demonstrated the effectiveness of squaraine-based probes in visualizing tumor progression and response to therapy in live animal models.[206] Furthermore, the combination of NIRF imaging with other modalities, such as positron emission tomography (PET),[207] enhances the overall diagnostic capabilities by providing both anatomical and functional information. The multimodal signal generation capability allows the use of squaraine based systems for a comprehensive understanding of tumor behaviour and treatment response, facilitating personalized medicine strategies.

SQ30-PSMA (prostate-specific membrane antigen) and **SQ31**-CN-PSMA (Fig. 15) are suitable candidates as pre-clinical *in vivo* bioimaging probes for prostate cancer.[208] The design structure and lack of aggregate formation improve the solubility in aqueous environments. The biocompatibility and emission at the NIR region enable the **SQ30**-PSMA and **SQ31**-CN-PSMA probes for deep tissue penetration, making them suitable agents for *in vivo* bioimaging. The optimized molecular design and absence of aggregate formation significantly enhance the solubility of the probes under aqueous conditions. The favourable biocompatibility and strong NIR emission of **SQ30-PSMA** and **SQ31**-CN-PSMA make them promising probes for *in vivo* applications.[208]

A nanocomplex (NC), namely, **SQ32**@BSA (Fig. 15), shows excellent biocompatibility upon dye–protein complex formation along with significant fluorescence enhancement, making it a suitable probe for high-resolution *in vivo* vascular imaging.[209] The acceptor-substituted **SQ32** undergoes co-assembly with BSA to form a dye–protein complex, which was dispersible in aqueous media. **SQ32**@BSA exhibits distinct absorption and emission peaks at 1070 and 1270 nm, respectively, indicative of its photophysical potential in the NIR-II window. These properties enable strong signal detection with minimal attenuation deep within biological tissues. Moreover, the nanoconjugates demonstrated

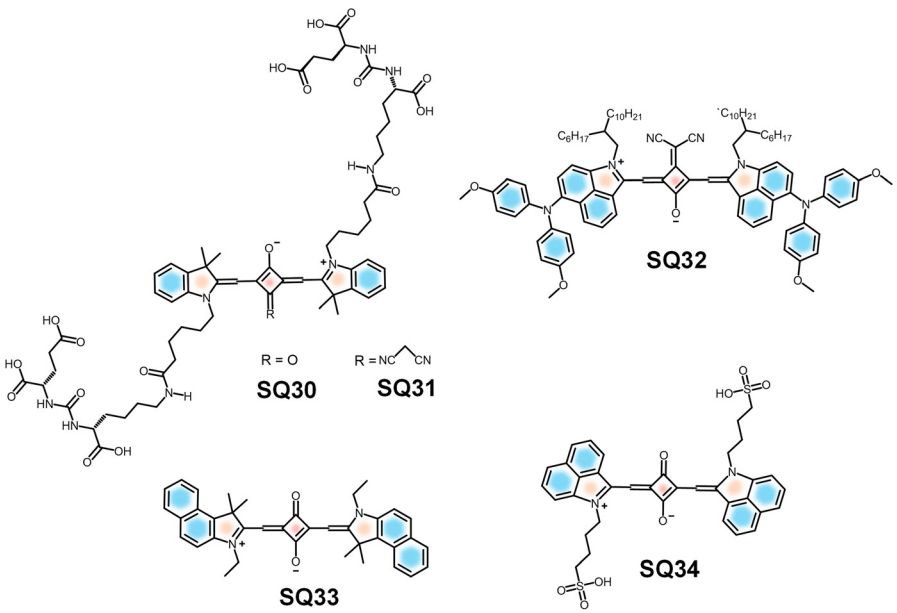

Fig. 15 Molecular structures of squaraine dyes reported for *in vivo* imaging studies.

biocompatibility and minimal toxicity, which makes them suitable probes for whole-body NIR-II imaging.[209]

Moreover, self-assembled nanoparticles (NPs) of a water soluble squaraine dye **SQ33** and the H-aggregates of dye **SQ34** (Fig. 16) were designed for the identification of tumor and lymph nodes *via in vivo* bioimaging.[42] Since **SQ33** does not form J-aggregates in aqueous solution, it exhibits strong fluorescence in both NIR-I and NIR-II regions under 660 nm excitation but not under 808 nm excitation. Whereas, **SQ34** did not respond to 660 nm excitation and emitted strong NIR-II fluorescence when excited at 808 nm, due to the H-aggregate formation through intermolecular π–π stacking. Due to this drastic absorption difference, the tumor and lymph node can be identified and distinguished by different excitation wavelengths.[42]

A novel quinoline-based squaraine dye **SQ35** (Fig. 16) was developed for near-infrared (NIR) fluorescence and photoacoustic imaging.[60] A dicyanomethylene modified center of the squarate bridge in **SQ35** leads to an improved photoluminescence quantum yield (PLQY) with a redshift in both absorption and emission wavelengths. **SQ35** was then encapsulated with the biocompatible surfactant Pluronic F-127, and as a result, micelle encapsulated **SQ35** with low cytotoxicity was formed. This micelle encapsulated **SQ35** exhibited characteristic NIR fluorescence intensity in Huh-7 cells and produced a strong signal in the thoracic and abdominal regions of mice, as illustrated in Fig. 16. Furthermore, the photoacoustic imaging capabilities of **SQ35** micelles were investigated, revealing a high signal intensity at 840 nm. Thus, the fluorescence and photoacoustic bimodal imaging capability of the new system underscores its promising potential for effective *in vivo* imaging.[60]

Furthermore, amphiphilic squaraine nanoprobes **SQ36** developed by encapsulating dyes within poly(maleic anhydride-*alt*-octadec-1-ene) (PMAO) nanoparticles displayed enhanced near-infrared (NIR) fluorescence stability in biological environments.[32] The dual lipophilization of dye **SQ36** and the polymer matrix boosts dye stability and emission efficiency, producing fine nanoprobes with adjustable surface properties for targeted cellular imaging. These nanoprobes have shown efficacy in sentinel lymph node mapping, representing a significant leap forward in *in vivo* diagnostics. Functionalization with amine groups provides additional options for customized applications in biomedicine, ranging from imaging to drug delivery.[32]

An organic–inorganic multifunctional nanocomposite, UC-IO/polymer-SQ, was reported by integrating upconversion nanoparticles (UCNPs), iron oxide nanoparticles (IONPs), and the squaraine dye for *in vivo* bioimaging and targeted drug delivery.[20] The dye exhibits distinct UV-vis absorption and fluorescence emission peaks around ~690 and 710 nm, respectively, which reflects its strong NIR signature. Through efficient resonance energy transfer with UCNPs, the composite shows multimodal imaging capabilities. This integrated imaging potential enhances both spatial resolution and diagnostic versatility in biological systems. Later, *in vivo* imaging was performed in mouse models by injecting 4T1 cells labelled with UC-IO/polymer-SQ, and then the multimodal imaging capability was tested. Strong UCL and PL signals were observed in tumors after 5 and 10 days of injection. The nanocomposite demonstrated excellent stability and biocompatibility, with predominant accumulation in the liver, spleen, and lungs, as confirmed by biodistribution studies. The UC-IO/polymer-SQ composite is a highly effective, biocompatible

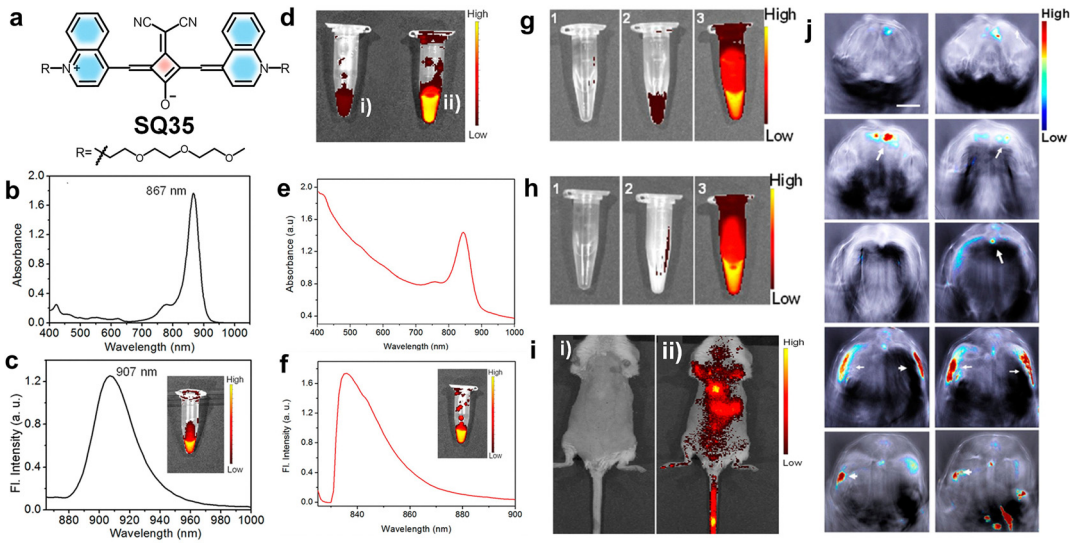

Fig. 16 (a) Structure of squaraine dye **SQ35**. (b) UV/vis absorption spectrum and (c) emission spectrum (ex. 840 nm) of **SQ35** in DMSO. (d) False-color pixel intensity of **SQ35** in (i) a 90% H_2O/DMSO mixture and (ii) in pure DMSO. (e) UV/vis absorption and (f) fluorescence emission spectra of $\mathbf{SQ35}_{micelle}$ in PBS. (g) and (h) False-color pixel intensity images showing the stability of **SQ35** and $\mathbf{SQ35}_{micelle}$ respectively. (i) Tracking of $\mathbf{SQ35}_{micelle}$ distribution in a live mouse before and after intravenous injection using the IVIS imaging system. Fluorescence reflectance images from the dorsal side of a female mouse were measured (i) before and (ii) after 2 min of intravenous injection with $\mathbf{SQ35}_{micelle}$. (j) Individual anatomy sections recorded after 35 min post-intravenous injection of $\mathbf{SQ35}_{micelle}$. Reproduced with permission from ref. 60, American Chemical Society, Copyright 2015.

platform for multimodal *in vivo* imaging and targeted drug delivery, offering significant potential for cancer theranostics.[20]

Cancer imaging and tumor assessment in live mouse models were performed using a preassembled squaraine molecular probe **SQ37Rot** (Fig. 18). Initially evaluations were conducted using single agent imaging (SAI), where separate cohorts of mice were administered either a targeted or non-targeting probe to compare imaging performance. To enhance robustness and reduce animal usage, a paired agent imaging (PAI) method was employed, where each mouse received a combination of two fluorescent probes with distinct emission wavelengths. This dual-probe approach offers simultaneous visualization of probe accumulation within the same tumor, thus improving data reliability and minimizing measurement errors. In addition, PAI was used to determine a targeted probe's binding potential (BP), which is a quantitative measure of its *in vivo* targeting effectiveness. The bioimaging analysis quantified the heterogeneous spatial distribution of integrin receptors within an individual tumor.[210]

Squaraine dyes for multiphoton bioimaging

Multiphoton bioimaging has revolutionized deep-tissue visualization by enabling high-resolution, 3D imaging with minimal photodamage and low background fluorescence.[211,212] Multiphoton excitation requires the quasi-simultaneous absorption of multiple photons, usually two or three, to fulfil the energy requirement for dye excitation.[213] However, the success of multiphoton imaging lies in the availability of fluorophores with high two-photon cross-sections, strong NIR emission and good photostability. The two-photon fluorescence microscopic technique (2PFM) offers unique advantages such as enhanced image contrast, image brightness and superior spatial resolution over conventional one-photon microscopy. Additionally, a significant reduction in light scattering and photodamage while imaging thick biological specimens such as tissue sections or organs makes it well-suited for bioimaging. Recent studies have identified several cyanine and squaraine derivatives with high two-photon absorption (2PA) cross-sections.[14] Among these, a few derivatives also exhibited liquid crystalline behaviour, which may further enhance their optical properties and facilitate ordered molecular arrangement in imaging systems.[14,214]

Squaraines such as **SQ36** have been developed to exhibit 2PA properties, making them suitable for 2PFM (Fig. 17). Here, an optical parametric generator is used to produce ultrafast pulses (~20 femtoseconds), enabling simultaneous excitation of the dye molecules by two NIR photons. The dye possesses an intense absorption at 688 to 706 nm; however, the non-linear excitation occurs at 840–1140 nm. This nonlinear excitation allows deep tissue penetration, reduced phototoxicity and enhanced 3D resolution compared to one-photon imaging.[14] Upon encapsulation of **SQ38** (Fig. 17) in PF-127 micelles, the hybrid shows enhanced photostability with minimal cytotoxicity favourable for bioapplications.[215]

The multiphoton imaging capabilities of a short squaraine dye (**SQ39**) (Fig. 17), having a symmetric structure with an indolenine end group as a donor moiety connected to squaric acid, have been investigated. Although **SQ39** exhibits weak two-photon excited fluorescence (TPEF) in aqueous media, a significant fluorescence enhancement (~17.7 fold) was observed upon complexation with bovine serum albumin (BSA) for signals at 850 nm and 1190 nm, respectively. Multiphoton imaging studies demonstrated effectiveness of the dye in both *in vitro* imaging of OVCAR-3 cells and *in vivo* imaging of mouse ear vasculature, leading to clear TPEF signals at tissue depths up to 100 μm. The dye exhibited excellent photostability at 1200 nm and low cytotoxicity, making it suitable for *in vivo* imaging studies. Therefore, combination of different synthetic

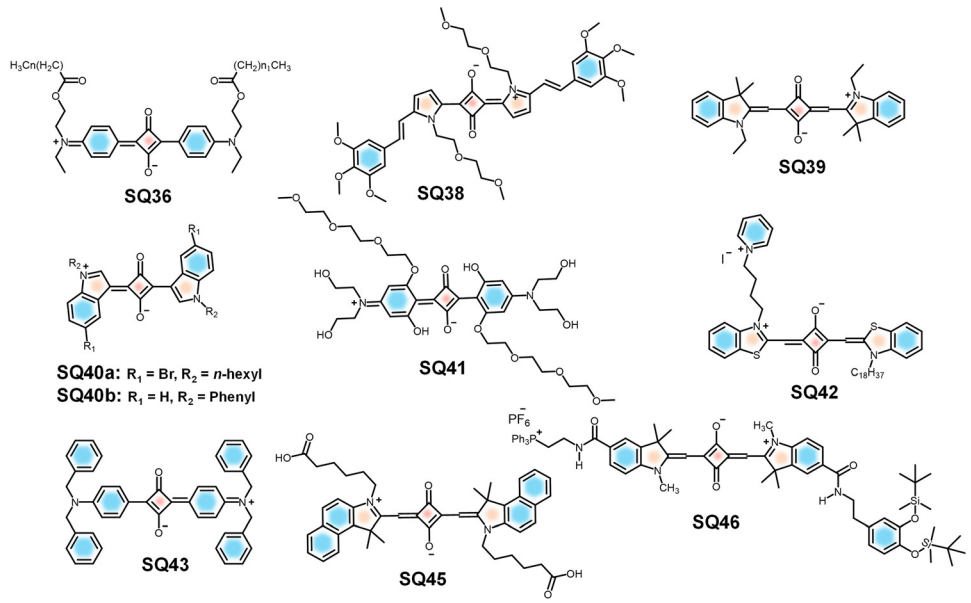

Fig. 17 Chemical structures of **SQ** dyes designed for *in vivo* imaging and multi-photon imaging applications.

approaches, enhanced TPEF performance with BSA, and robust photostability make it a highly promising probe for long-term, deep-tissue multiphoton bioimaging in the NIR-II region.[216]

Indolic squaraine dyes (**SQ40**) represent a class of small organic dyes with large (TPA) cross-sections (δ). The multiphoton imaging potential of (**SQ40s**) was examined, focusing on **SQ40a** and **SQ40b**, having alkyl and phenyl substitutions, respectively, enhancing their two-photon absorption (TPA) cross-sections.[217] These dyes exhibit large TPA cross-sections, among which **SQ40a** shows a remarkable TPA value of approximately 1200 GM, attributed to its conjugated structure and favourable energy gaps. Multiphoton imaging was demonstrated using **SQ40b** for two-photon excited fluorescence (TPEF) in TPC/SM tracing of blood flow in mouse brain vessels; a confocal microscope with a femtosecond laser gives high-resolution imaging in one stem and two branch vessels. The dyes' strong TPEF and their molecular design allow effective visualization of dynamic biological processes.[217]

ermore, a study conducted on squaraine **SQ41** and a charged benzothiazole-based squaraine derivative **SQ42** revealed multiphoton imaging capabilities (Fig. 17). Both dyes showed large two-photon absorption (2PA) cross-sections due to their conjugated structures and electronic symmetry.[218] These dyes exhibited strong fluorescence and photochemical stability, with **SQ42** displaying brightness in two-photon excited fluorescence (TPEF) imaging. Multiphoton imaging was performed using a femtosecond laser system, enabling high-resolution visualization of HeLa cells incubated with **SQ42**. These findings suggest that both squaraines, particularly **SQ42**, are promising candidates for two-photon fluorescence bioimaging owing to their enhanced 2PA properties and bright fluorescence, offering potential for advanced biological imaging applications.[218]

Squaraine for photoacoustic imaging

Photoacoustic tomography (PAT) is a non-invasive imaging modality that offers higher resolution and significantly greater penetration depth compared to other optical imaging techniques.[15,219] This technique involves the local absorption of radiation within tissues, leading to transient thermoelastic expansion.[220] This expansion generates pressure waves that can be detected with an ultrasound transducer. Photo-acoustic imaging provides a powerful complement to conventional imaging methods by integrating the high spatial resolution of optical imaging with the deep tissue penetration capabilities of ultrasound.[221,222] The combination of these modalities enables researchers to gain a more comprehensive understanding of biological processes, particularly in complex tissues such as tumours.[223]

In this context, squaraine dyes have emerged as promising photoacoustic (PA) chromophores due to their tunable photophysical properties in the NIR window (Scheme 3a). Based on the absorption characteristics and excited-state lifetime (τ) relative to the laser pulse (τ_{laser}) duration, these dyes can be categorized into three distinct types. Type 1 chromophores exhibit linear-absorption with rapid $S_1 \rightarrow S_0$ decay ($\tau \ll \tau_{laser}$), resulting in minimal excited-state absorption and enhanced PA efficiency (Scheme 3b). Type 2 chromophores display saturable-absorption ($\tau \gg \tau_{laser}$) with negligible excited-state absorption, leading to reduced PA signals with higher photobleaching risk (Scheme 3b). Type 3 chromophores undergo nonlinear-absorption with long-lived excited states ($\tau \gg \tau_{laser}$) characterized by significant excited-state absorption that enables nonlinear PA signal amplification under increasing laser energy.

The favourable intense NIR absorption of squaraines combined with their good photostability underscores their potential

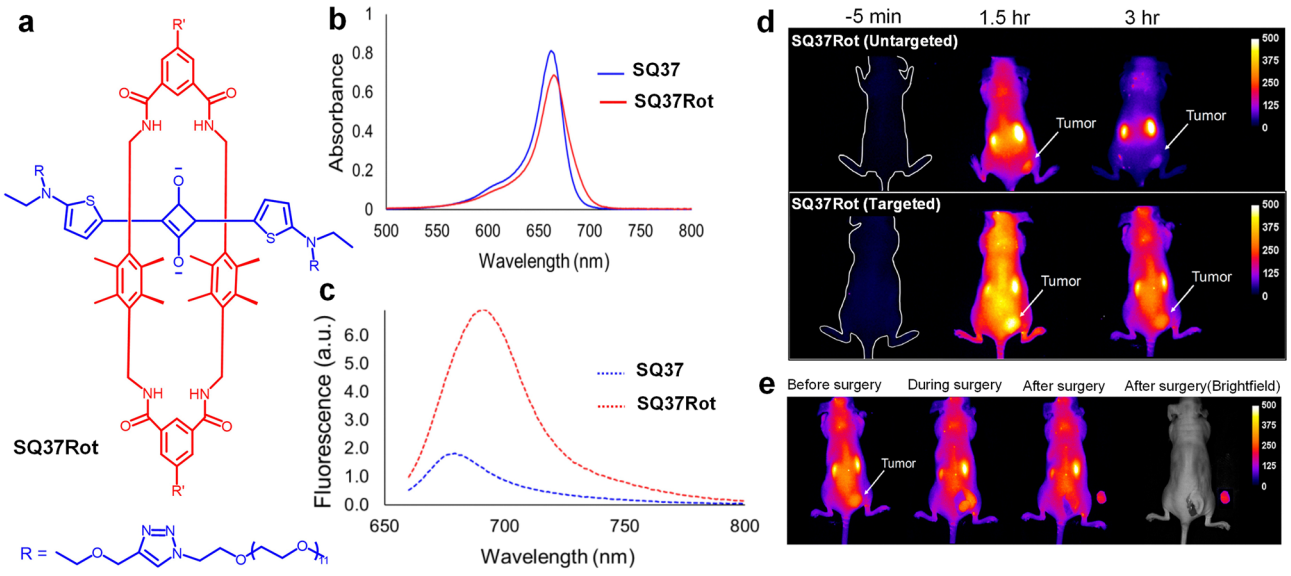

Fig. 18 (a) Structure of squaraine dye **SQ37Rot** (R′ = cyclic peptide with the sequence cRGDfK). (b) UV/vis absorption spectrum and (c) emission spectrum of **SQ37** and **SQ37Rot**. (d) Fluorescence images of tumor-burdened mice at −5 min, 1.5 h, and 3 h, following intravenous injection of **SQ37Rot**. (e) Mock surgical images of tumor-bearing mouse 3 h post-injection of **SQ37Rot**, captured sequentially, before surgery, during surgery, and after surgery. Reproduced with permission from ref. 210, American Chemical Society, Copyright 2019.

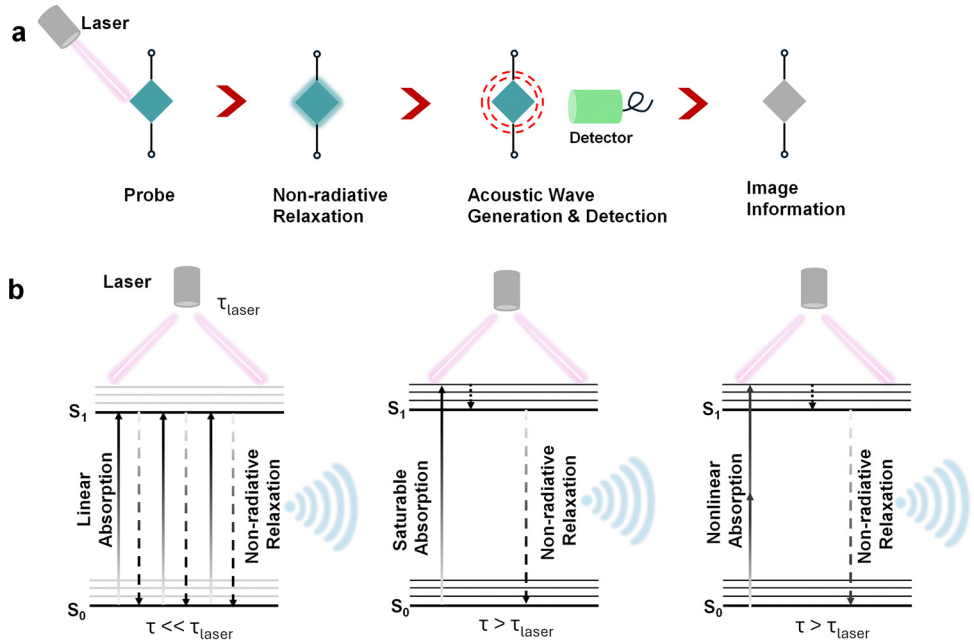

Scheme 3 Schematic representation of the (a) principle and (b) mechanism of photoacoustic signal generation.

as contrast agents for photoacoustic imaging. A NIR-absorbing nanocomplex composed of a squaraine dye (**SQ43**) (Fig. 17) and albumin exhibited enhanced photoacoustic tomography (PAT) performance *in vivo*.[15] The **SQ43** dye exhibits aggregation-induced NIR absorption, with a red-shift from 632 nm to the 700–900 nm tissue-transparent window, making it an effective PAT contrast agent due to its strong light absorption and stability (Scheme 3b). However, **SQ43** aggregates exhibit poor solubility under aqueous conditions; therefore, albumin was introduced as a protective carrier (Fig. 17). The **SQ43**–albumin nanocomplex not only preserves the red-shifted NIR absorption of the **SQ43** aggregates but also forms stable dispersion in aqueous solutions. For PAT imaging, the **SQ43**–albumin nanocomplex was injected into Balb/c mice. Upon irradiation with a pulsed laser (710–800 nm), thermoacoustic signals were generated, which were detected by an ultrasound transducer, enabling high-resolution imaging of the liver and tumors with minimal background noise from vasculature.[15]

Multimodal bioimaging using squaraine dyes

Multimodal imaging of metastatic breast cancer has been achieved by the use of squaraine dye **SQ44**. Interestingly, this probe enables NIR-II imaging, photoacoustic (PA) imaging, and photothermal therapy within a single platform. The **SQ44** nanoprobe exhibits photostability, deep tissue penetration, and efficient photothermal properties, making it a promising theranostic tool for metastatic breast cancer. **SQ44** displayed a red-shifted absorption peak at 940 nm and a fluorescence peak at 980 nm, positioning it well within the NIR-II region (Fig. 19). For photoacoustic imaging, excitation of the nanoprobe at 915 nm using NIR laser generates acoustic signals to produce high-resolution images, with PA intensity linearly correlating with molar absorptivity of the nanoprobe. The integration of NIR-II fluorescence and PA imaging enhances the precision of tumor visualization, facilitating accurate detection of both primary breast tumors and lung metastases in murine models (Fig. 20).[69]

A benzindole-based squaraine dye (**SQ45**-RGD) was developed for bimodal photoacoustic (PA) and near-infrared (NIR) fluorescence imaging of αvβ3 integrin-overexpressing tumors (Fig. 17). **SQ45**-RGD, conjugated with cyclic arginine-glycine-aspartic acid (cRGD) peptides to enable targeted delivery, exhibits strong NIR absorption above 600 nm and enhanced PA signal generation.[41] For *in vivo* imaging, **SQ45**-RGD was administered to M21 tumor-bearing mice followed by NIR laser irradiation to induce acoustic signals, which were then subsequently detected to produce high-resolution tumor images. **SQ45**-RGD shows higher tumour accumulation compared to non-targeted **SQ45**. The combined PA and NIR fluorescence imaging capabilities in murine xenograft models underscore the potential of **SQ45**-RGD as an advanced diagnostic tool for cancer imaging.[41]

Yet another innovative approach was experimented using **SQ46Rot** integrated with superparamagnetic Fe_3O_4 nanoparticles (**SQ46RotNPs**), representing an advanced strategy for multimodal imaging (Fig. 17). The complementary strengths of NIR fluorescence from **SQ46Rot** and magnetic resonance imaging (MRI) were achieved using this method. The system incorporates sugar-functionalized mechanically interlocked molecules (MIMs) that boost the NIR fluorescence efficiency and durability of an asymmetrical squaraine dye.[224] Dual-functional stoppers promote targeted accumulation in the mitochondria *via* a lipophilic cationic triphenyl phosphonium (TPP^+) group and a dopamine anchor. Furthermore, the use of click chemistry modification improved the water solubility of the conjugates, allowing real-time imaging in living cells.

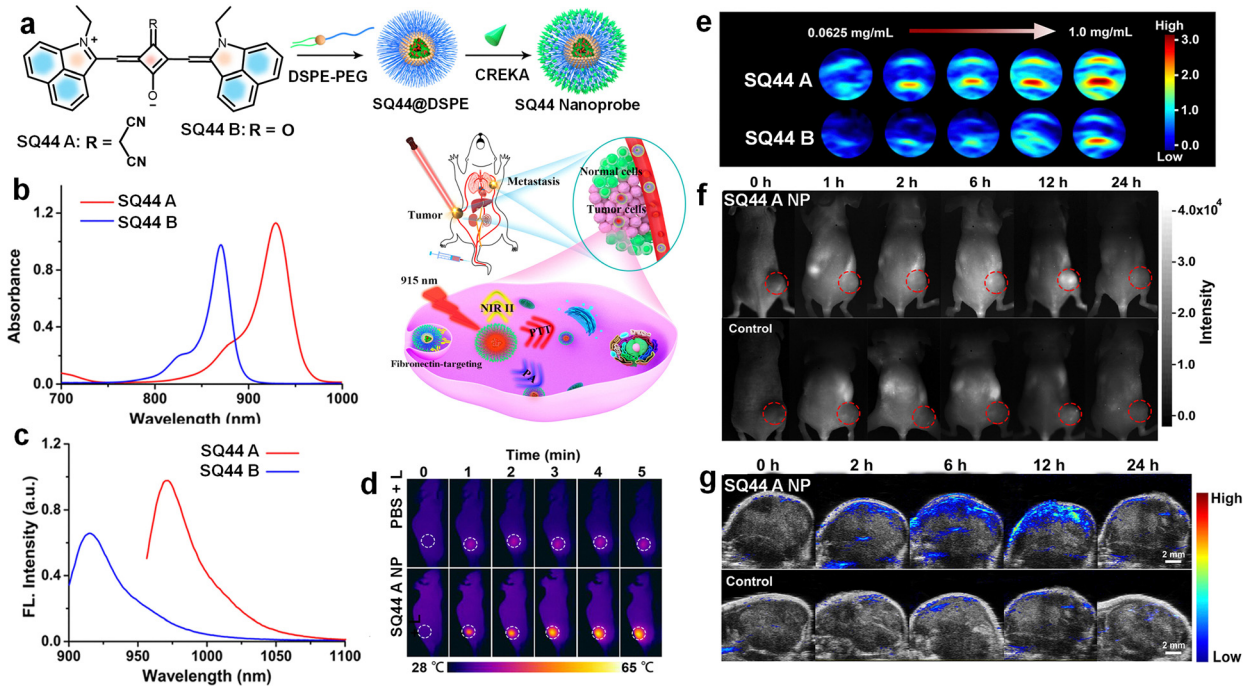

Fig. 19 (a) Schematic illustration of generation of the **SQ44** nanoprobe. (b) UV/vis absorption and (c) emission spectra of **SQ44 A** and **SQ44 B** in THF. (d) Thermal imaging of tumors postinjection of PBS or the **SQ44 A** NP combined with laser irradiation. (e) PA images (at 930 nm) of **SQ44 A** and **B** nanoprobes at 0.0625, 0.125, 0.25, 0.5, and 1.0 mg mL^{-1}. (f) NIR-II imaging and (g) PA imaging of fibronectin-positive MDA-MB-231 tumors at 0, 1, 2, 6, 12, and 24 h postinjection of the **SQ44 A** nanoprobe or control intravenously. Reproduced with permission from ref. 69, American Chemical Society, Copyright 2020.

Beyond diagnostics, this platform holds promise for therapeutic applications through hyperthermia, highlighting the versatility and clinical potential in biomedical imaging and therapy.[224]

As mentioned earlier, an *in vivo* bimodal imaging study on seven-week-old female severe combined immune deficiency (SCID) mice was performed to evaluate the performance of **SQ6** in detecting aminothiols using fluorescence and photoacoustic imaging techniques. Fluorescence imaging was performed on fasting mice, followed by photoacoustic imaging after administering **SQ6** (2 mM, 200 μL). Strong red fluorescence appeared at 15- and 40-minutes post-injection, indicating **SQ6** distribution in the bloodstream and abdominal region. After feeding, fluorescence signal intensity was found to be decreased, suggesting increased concentration of thiol, which reacts with **SQ6**. Photoacoustic imaging confirmed abdominal accumulation and revealed higher aminothiol levels post-feeding through a spectral unmixing approach. This dual imaging strategy shows promise for non-invasive detection of aminothiols, potentially aiding early diagnosis of diseases such as coronary heart disease.[153]

Theranostic and therapeutic applications of squaraine dyes

The dual-functionality approach that integrates diagnostics and therapy into a single platform referred to as 'theranostics' has undergone rapid advancement in recent years. The theranostic approach is particularly valuable in oncology, where precise imaging and targeted treatment are essential for effective disease management.[225,226] A wide collection of molecular materials have been tested for theranostic applications, including organic dyes, small molecules, polymeric materials, nanomaterials, carbon-based materials, and hybrid as well as multifunctional systems.[227,228] These platforms offer diverse capabilities for simultaneous disease detection, monitoring and treatment.

In a recent study, squaraine dyes **SQ33** and **SQ34** were reported for multiplexed *in vivo* imaging and photothermal therapy (PTT) within NIR-I and II windows (Fig. 15). In the PTT experiments, the dyes were administered to tumor-bearing mice and irradiated with an 808 nm laser, causing the dyes to absorb NIR light and convert it into heat. The process elevated the tumor temperatures from 18 to 34 °C, inducing localized hyperthermia and effective cancer cell ablation. The study highlighted the ability of the dye to form H-aggregates, which enhanced their photothermal effects, and demonstrated their low cytotoxicity and high biocompatibility. **SQ33** and **SQ34** nanoparticles exhibited strong efficacy in both PTT and multiplexed imaging, indicating their potential as precise and targeted agents for advanced cancer therapy.[42]

Similarly, **SQ45** exhibits strong absorption and fluorescence in the range of 650–750 nm. High molar extinction coefficients and enhanced photostability make it suitable for PDT despite its poor water solubility. In PDT, **SQ45** is delivered to HT-29 colorectal adenocarcinoma cells often using bovine serum albumin (BSA) as a carrier to enhance tumor targeting for the enhanced permeability and retention (EPR) effect. Upon 671 nm laser irradiation, **SQ45** generates reactive oxygen species (ROS) through Type I (radical species) and Type II (singlet oxygen)

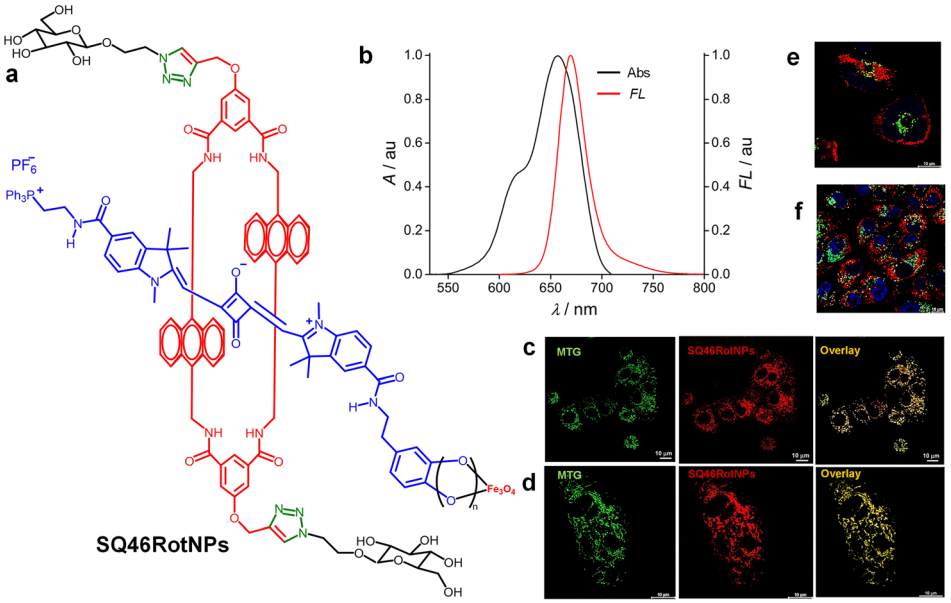

Fig. 20 (a) Structure of squaraine rotaxane on Fe_3O_4 nanoparticles (**SQ46RotNPs**). (b) UV/vis absorption spectrum (black) and fluorescence (red) spectrum of **SQ46RotNPs**. CLSM images of **SQ46RotNPs** colocalized with MitoTracker green in live (c) HeLa and (d) A549 carcinoma cells. Multicolor CLSM images of living (e) HeLa and (f) A549 cancer cells. Reproduced with permission from ref. 224, American Chemical Society, Copyright 2023.

mechanisms, inducing significant cancer cell death *via* apoptosis and necrosis. However, the **SQ45**'s fluorescence signal decreases post-irradiation due to photodegradation, indicating the need for improved tumor detection. **SQ45** combined with laser irradiation is a highly effective photosensitizer for PDT, offering promising potential for targeted cancer therapy with enhanced tumor suppression.[229]

Notably, squaraine-based semiconducting polymer nanoparticles (**SQ47-DBCO**) were developed as a high-performance theranostic platform. Featuring a donor–acceptor structure with extended π-conjugation, these nanoparticles enable 1064 nm excitation for dual NIR-II fluorescence imaging (FI) and NIR-II photothermal therapy (PTT). **SQ47-DBCO** allows deep-tissue penetration by exhibiting absorption at 882 nm and significantly redshifted emission at 1290 nm within the low-autofluorescence NIR-II window. The theranostic activity of **SQ47-DBCO** is elevated through bioorthogonal click chemistry, where surface dibenzocyclooctyne (DBCO) moieties covalently bind azido groups pre-installed on tumor cells with Ac_4ManNAz. This targeted approach yields a 2.5-fold enhancement in the tumor signal-to-background ratio (up to 7.06), and therefore **SQ47-DBCO** enables real-time NIR-II FI and PTT in colorectal tumor-bearing mice. The high photothermal conversion efficiency of 33.4% by maintaining excellent photostability, biocompatibility and a near-complete tumor suppression make this dye a promising tool in the field of theranostics.

Photodynamic therapy

Squaraine dyes can generate reactive oxygen species (ROS) upon NIR excitation due to their unique photophysical characteristics.[230] Upon excitation, π-conjugated squaraine molecules act as photosensitizers, which undergo intersystem crossing from the excited singlet state to the triplet state.[230,231] The excited species in the triplet state possess longer lifetime and allows energy transfer to molecular oxygen (O_2), abundant in malignant cells. This transfer of energy generates extremely reactive singlet oxygen ($^1O_2$) (Scheme 4), which upon interaction with biological cells/tissues induces oxidative damage and ultimately cellular apoptosis.[232–234] The ability of squaraine derivatives to produce ROS under NIR excitation makes them particularly valuable for photodynamic therapy (PDT) of deep-seated tumours with minimal invasiveness.[235]

Halogenated squaraine dyes, specifically bromo substituted **SQ48** and its iodine appended analogue **SQ49** (Fig. 21), were developed to investigate their efficacy in PDT for inducing cytotoxicity and DNA damage in the presence of light (>600 nm).[236] Both dyes efficiently generate single-strand breaks (SSBs). Oxidative DNA base modifications in PM2 DNA and ASS3 Chinese hamster ovary cells with **SQ48** produce higher levels of 8-oxo-2′-deoxyguanosine (8-oxoG) compared to **SQ49**. The underlying mechanism involves Type III sensitized reactions, in which singlet oxygen and radical intermediates play key roles, as evidenced by enhanced SSB formation in the presence of H_2O_2 and D_2O. Owing to their favourable photophysical and photobiological properties **SQ48** and **SQ49** show promise as PDT agents for treating superficial tumors and vascular abnormalities. However, the therapeutic potential of these derivatives is constrained by issues related to aggregation and photodecomposition, which demand further structural optimization.[236]

Similarly, a brominated squaraine derivative (**SQ50**) (Fig. 22) was integrated into cholesterol–stearalkonium quatsomes (QS) as a photosensitizer for photodynamic therapy (PDT).[237] When loaded into QS, **SQ50** overcomes its poor water solubility and aggregation-induced quenching to show a high molar extinction

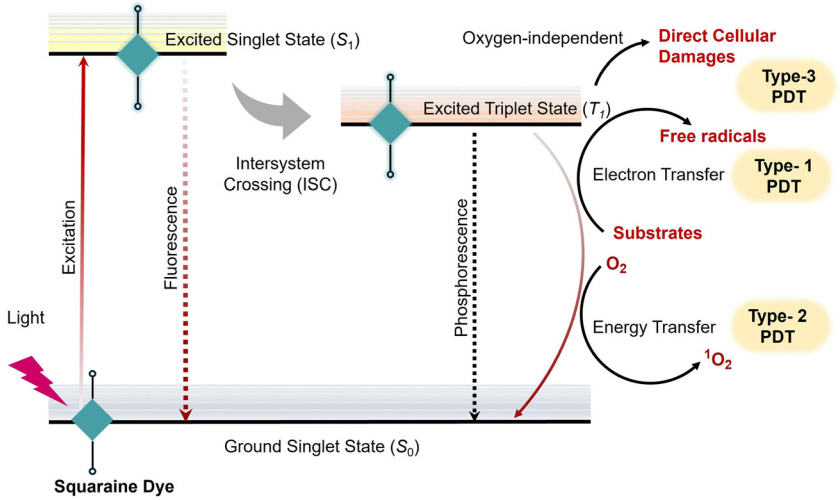

Scheme 4 Illustration of the excitation process of SQ dyes and the mechanism involved in photodynamic therapy applications.

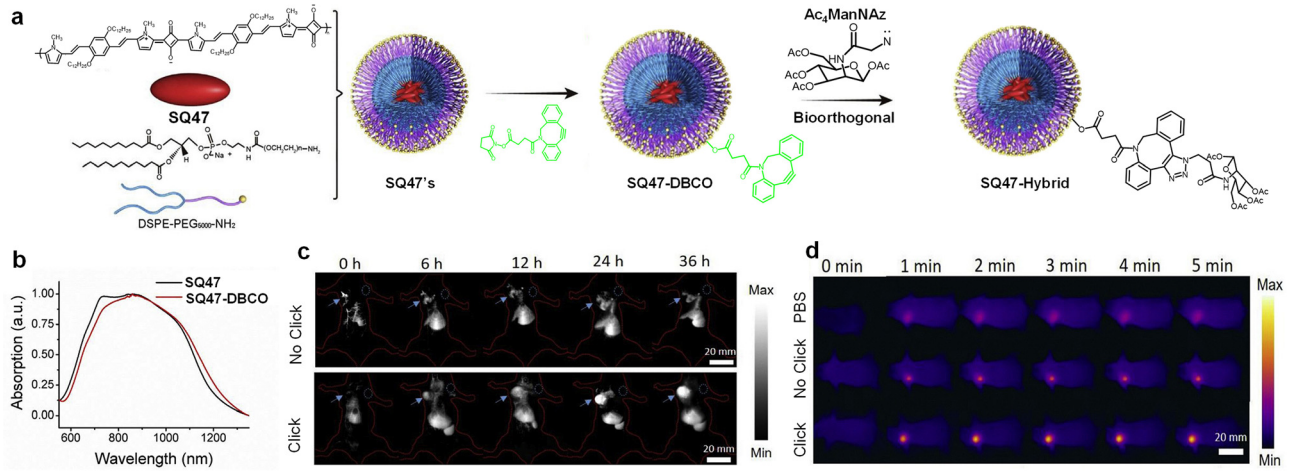

Fig. 21 (a) Structure of squaraine dye **SQ47**, illustration of the reaction mechanism of **SQ47-DBCO** and Ac4ManNAz. (b) NIR absorption spectra of **SQ47** and **SQ47-DBCO**. (c) *In vivo* NIR-II images of mice in the no-click group and click group (pretreated with intratumoral injection Ac4ManNAz for 3 days) after *via* injection of **SQ47-DBCO**. (d) Photothermal photographs of mice in the three groups (PBS, no-click and click) exposed to a 1064 nm laser. Reproduced with permission from ref. 76, Elsevier, Copyright 2020.

coefficient and absorption at 644 nm in aqueous media. 660 nm light activates **SQ50**-loaded QS, producing reactive oxygen species (ROS) through Type I and II reactions that cause MCF-7 cancer cells to undergo necrosis and apoptosis. Effective PDT is achieved at 10–1000 times lower dye concentrations than the free dye (0.1–1 μM) with minimal dark toxicity, thanks to the QS system, which also improves cellular uptake and phototoxicity.[237]

SQ51 exhibits a high singlet oxygen quantum yield and strong absorption in the 600–700 nm range (Fig. 21). When adsorbed onto chitosan (a linear polysaccharide derived from chitin), the stability of the dye is enhanced and the fluorescence quantum yields and lifetimes (3.75–3.99 ns) of the dye improved, indicating the minimization of the nonradiative decay pathways.[238] Upon 640 nm excitation, **SQ51** generates reactive oxygen species that induce necrosis and apoptosis in HeLa cells. The dye exhibits low dark toxicity and high phototoxicity; therefore, **SQ51**/chitosan demonstrated its potential as a potent PDT agent. Furthermore, the favourable photophysical properties of the hybrid support targeted cancer treatment with minimal side effects, offering low dark toxicity, potent light-induced cytotoxicity, and potential for targeted cancer therapy due to its favourable photophysical properties.[238]

In another study, the indolenine-based amino-squaraine dyes (**SQ52**), evaluated across multiple tumor cell lines, revealed significant photodynamic activity and singlet oxygen generation capability.[239] Similarly, unsymmetrical squaraines derived from quinoline and benzoselenazole exhibited selective cytotoxicity and enhanced ROS production, highlighting their potential for PDT applications. Studies investigating the interaction of squaraine dyes with DNA and their ability to bind externally and displace groove binders paved the way for future PDT probe development. Squaraine dyes have also been utilized for dual functionalities,

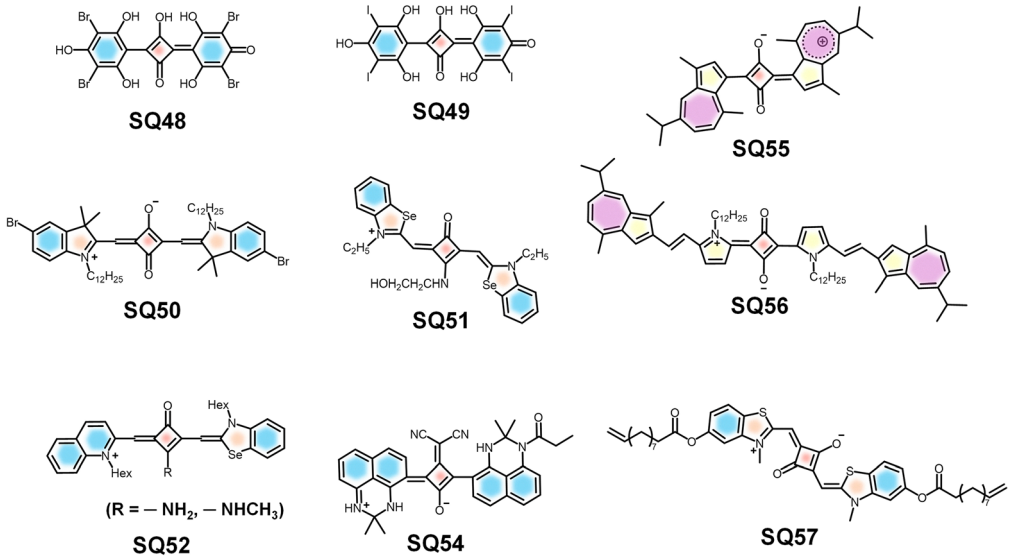

Fig. 22 Molecular structures of **SQ**s designed for theranostic applications.

such as photoacoustic imaging and photothermal therapy. Azulene-containing squaraines displayed efficient NIR absorption and photothermal conversion, enabling simultaneous tumor imaging and therapy. These multifunctional systems underscore the versatility of squaraine dyes in theranostic platforms.[239]

Squaraine-rotaxane dyes have immense potential in photodynamic therapy (PDT). They are sterically protected dyes that maintain or enhance the photophysical properties of the parent squaraines and are much more stable, especially in biological fluids.[240] Halogenated squaraine-rotaxane systems exhibit enhanced resistance to photooxidation and function as more efficient triplet photosensitizers. Therefore, the iodinated squaraine rotaxane **SQ27** (Fig. 12) has been used as a photosensitizer to generate singlet oxygen without much degradation. Studies on iodinated squaraine dyes revealed that they do not exhibit the expected absorption broadening upon aggregation in aqueous solutions. The efficiency of generation of singlet oxygen was measured by trapping with 1,3-diphenylisobenzofuran, which indicated that squaraine-rotaxanes have more potential as singlet oxygen generators for PDT compared to conventional halogenated squaraines.[240]

Photothermal therapy (PTT)

Photothermal therapy (PTT) is another promising approach in cancer treatment that utilizes light energy to generate localized hyperthermia for the destruction of diseased tissues, commonly cancerous tumors.[241,242] The process involves applying photothermal agents capable of absorbing light and converting to thermal energy. By making use of the intrinsic properties of the materials, PTT agents raise the temperature of the surrounding tissues, which further induces cellular damage through mechanisms such as protein denaturation, membrane disruption and apoptosis.[243,244] Nanoparticles, such as gold nanoshells and magnetite nanoparticles, have been extensively studied for their ability to generate heat upon NIR irradiation, making them ideal candidates for PTT applications.[245,246] The effectiveness of PTT is significantly influenced by the design of the nanoparticles used. For instance, gold nanoshells can be tailored to specific sizes and shapes to optimize their optical properties for efficient heat generation.[247,248] Additionally, the combination of PTT with imaging modalities allows for real-time monitoring of treatment responses, enhancing the overall therapeutic strategy. The integration of PTT with other treatment modalities, such as PDT, has shown synergistic effects, leading to improved therapeutic outcomes in preclinical models.[249]

On the other hand, excitation of squaraine derivatives, especially in aggregated or nanoparticle-encapsulated forms, results in a non-radiative decay process that generates localized heat suitable to generate hyperthermia-induced cell death. The low fluorescence quantum yield in aggregated states implies non-radiative thermal conversion over radiative emission. In addition, squaraines can be chemically modified or incorporated into nanocarriers to improve water solubility, biocompatibility and tumor targeting capabilities as discussed in previous sections. For example, squaraine dye **SQ53** nanoparticles (NPs) exhibit strong near-infrared (NIR-II) absorption at 1000 nm, a high photothermal conversion efficiency (PCE) of 86.3%, and excellent photothermal stability, making them ideal for PTT (Fig. 23). During PTT, **SQ53** NPs were administered to tumor-bearing mice, where they accumulate in tumors *via* the enhanced permeability and retention effect (EPR). Upon activation by 1064 nm laser irradiation, the NPs generate heat, raising tumor temperatures to 58.8 °C, sufficient for effective tumor ablation. *In vivo* experiments conducted on melanoma cells and tumor-xenografted mice demonstrate significant tumor rapture without recurrence, as confirmed by TUNEL staining, with no notable toxicity in major organs. **SQ53** NPs proved to be highly effective and safe for NIR-II PTT, offering a promising approach for targeted cancer therapy.[81]

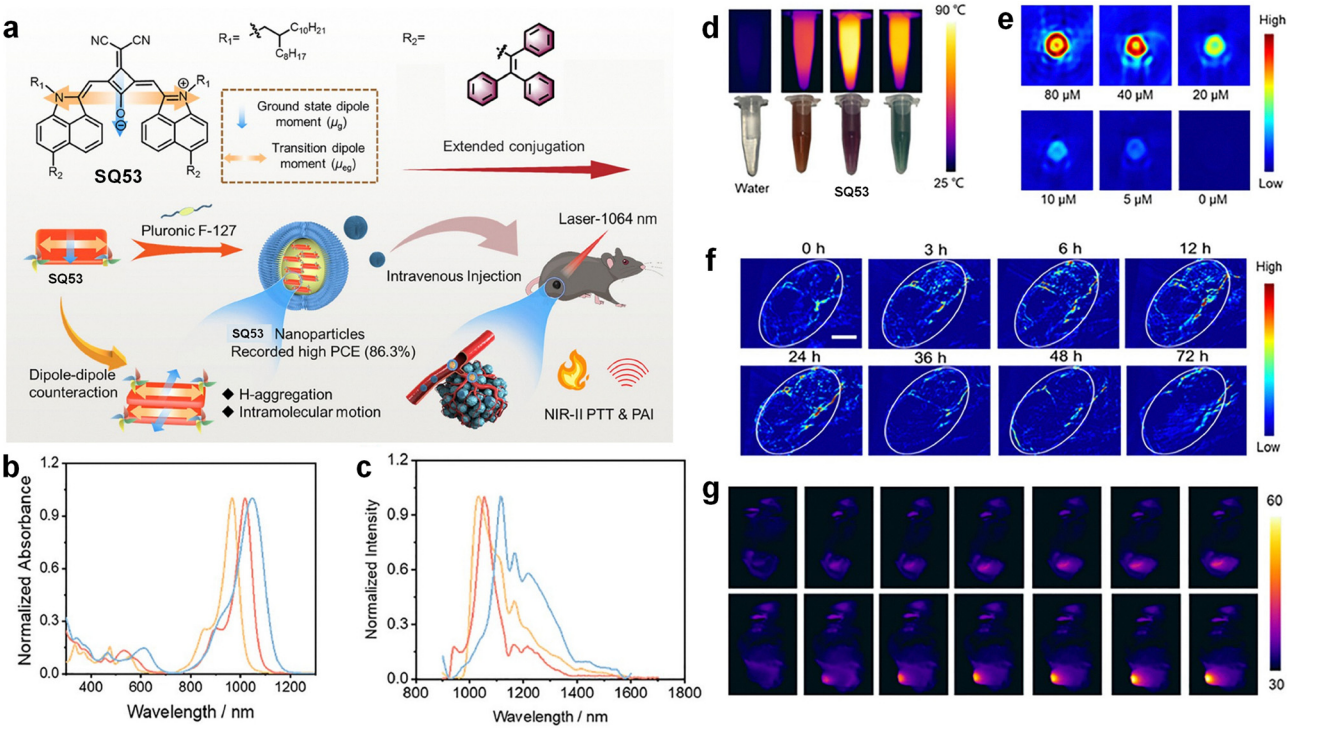

Fig. 23 (a) (I) Structural properties of **SQ53**; (II) schematic illustration of self-assembly and PTT guided by photoacoustic (PA) imaging using **SQ52** nanoparticles. (b) UV/vis absorption spectrum (red) and (c) photoluminescence (red) of **SQ53**. (d) Photothermal images of **SQ53** NPs and water under laser irradiation. (e) PA images at different concentrations of **SQ53** NPs. (f) PA images of tumors after intravenous **SQ53** NP injection. (g) Infrared thermal imaging of B16-F10 tumor-bearing mice treated with saline or **SQ53** NPs and exposed to 1064 nm laser. Reproduced with permission from ref. 81, Science China Press, Copyright 2023.

In another study, nanoparticles that utilize squaraine dye **SQ54** for enhanced photothermal therapy (PTT) applications were developed.[223] The therapy involves irradiating the nanoparticles with NIR light (830 nm), which they absorb and convert into heat, effectively ablating cancer cells through localized hyperthermia. It was demonstrated that these

Table 1 Comparison of photophysical properties of SQ with other organic dyes

Probes	Excitation/emission	Quantum yield (%)	Applications	Ref.
Squaraine (SQ)	630–1142 nm/1290 nm	0.47	Bioimaging, biosensing, photodynamic therapy, photothermal therapy, and drug delivery	1, 12, 17, 20 and 28
Indocyanine green (ICG)	787 nm/819 nm	0.09–0.14	Medical imaging (angiography) and fluorescence-guided surgery	113 and 114
Cyanine (Cy5)	650 nm/670 nm	0.27	Fluorescence labeling, microscopy, DNA staining, and *in vivo* imaging	115 and 116
Phthalocyanine	600–700 nm/690–720 nm	0.6	PDT, dye-sensitized solar cells, and gas sensors	117 and 118
BODIPY	420–520 nm/40–580 nm	0.7–0.9	Fluorescent sensors, lasers, bioimaging, theranostics, and super-resolution microscopy	119 and 120
Curcumin	430 nm/500–550 nm	—	Food coloring, antioxidant sensors, and phototherapy	121 and 122
IR-1061-PEG nanoparticles	808 or 980 nm/ 1000–1400 nm	1.8	Inner organs and blood vessels	123
SPN1	808 nm/1050–1350 nm	1.7	Cancer cells and arterial blood flow	124
SCH1100	808 nm/1100 nm	0.2	Prostate cancers	125
FD-1080	1064 nm/1080 nm	0.31	Hindlimb vasculature, brain vessel, and respiratory cranio-caudal motion of liver	126
CH1055	808 nm/1055 nm	0.3	SLN, orthotopic glioblastoma brain tumor, brain vasculature and imaging guided tumor surgery	127
IR-E1	808 nm/1071 nm	0.7	TBI-induced hemodynamic abnormalities and cerebrovascular damage	128
IR-FEP	808 nm/910 and 1100 nm	2.0	Blood flow in hindlimb and tumors	129
IR-FEPC	808 nm/1100 nm	2.6	Adult female ovary in living mice	130
IR-FG	808 nm/1050 nm	1.9	Histological tissue staining	131
IR-FTAP	808 nm/1048 nm	5.3	Blood vessels of a mouse hindlimb	132

nanoparticles achieve high photothermal conversion efficiency, enhancing their therapeutic efficacy. The tailored design of **SQ54** was found to offer significant potential for precise and effective PTT, paving the way for advanced cancer treatment strategies.

Azulene-containing squaraine dyes, particularly **SQ55** and **SQ56**, show significant PTT capability (Fig. 22). These dyes feature a zwitterionic structure with a conjugated π-system in a "D–A–D" configuration, which enhances NIR absorption and photothermal conversion efficiency due to intramolecular charge transfer. For PTT applications, **SQ55** and **SQ56** nanoparticles were administered to 4T1 tumor-bearing mice and irradiated with an 808 nm laser at 1 W cm^{-2} for 5 minutes, converting absorbed NIR light into heat to induce localized hyperthermia, effectively ablating cancer cells.

Table 2 Summary of squaraine dyes and their applications

Dye	Applications	Absorption/emission (nm)	Ref.
SQ1	Sensing of adenosine triphosphate	547–627/650	148
SQ2	Sensing of adenosine triphosphate	670/700	147
SQ3	Sensing of cyclic phosphate	≈625/≈ 675	150
SQ4	Sensing of pyrophosphate and alkaline phosphatase	590–640/650	151
SQ5	Sensing of amino thiols in human blood plasma	440/592	152
SQ6	NIR imaging for the detection of amino thiols, photoacoustic imaging, and *in vivo* imaging in mice	680/705	63 and 153
SQ7	Sensing of cysteine (Cys) and glutathione (GSH)	631/662	155
SQ8	Detection of carbonic anhydrase	620–636/≈ 640	156
SQ9	Detection of G-quadruplexes	685/710	158
SQ10	Detection of G-quadruplexes	650/675	158
SQ11	Detection of human serum albumin (HSA) in blood	660/675	159
SQ12	Detection of bovine serum albumin (BSA) in blood	630/660	160
SQ13	Labelling of oligonucleotides	654–665/668–671	161
SQ14	Detection and imaging of the activities of leucine aminopeptidase	650/710	162
SQ15	Detection of neutrophil extracellular traps	680/720	163
SQ16	Detection of Ca^{2+} ions	630/652	165 and 166
SQ17	Detection of Cu^{2+} ions	514/—	170
SQ18	Detection of Cu^{2+} ions	554/—	170
SQ19	Detection of Cu^{2+} ions	675/—	52
SQ20	Detection of Pb^{2+} ions	642–660/658–680	171
SQ21	Detection of Al^{3+} ions	≈420/505	175
SQ22	Detection of Hg^{2+} ions	630/660	178 and 179
SQ23	Near-infrared (NIR) fluorescence-guided surgery (FGS) in epithelial ovarian cancer	—	191
SQ24	Near-infrared fluorescence imaging of foetal bovine serum	720/734	192
SQ25	Near-infrared fluorescence imaging and detection of intracellular pH changes	681/702	193
SQ26	Targeted fluorescence imaging of the bone	660/667	201
SQ27	Photodynamic therapy	642/673	240
SQ28 Rot	Near-infrared fluorescence imaging of live Chinese hamster ovary (CHO) cells	652/670	203
SQ29	Near-infrared fluorescence imaging of HeLa cells and targeted drug delivery	569/596	204
SQ30, SQ31	*In vivo* imaging of prostate cancer	642/650 and 678/706	208
SQ32	*In vivo* vascular imaging	1270/—	209
SQ33	*In vivo* imaging of tumour and lymph nodes	725/907	42
SQ34	*In vivo* imaging of tumour and lymph nodes	858/905	42
SQ35	Bimodal imaging of tumour and lymph nodes	867/907	60
SQ36	*In vivo* imaging and cellular imaging	688–706/840–1140	32
SQ37 Rot	*In vivo* imaging of tumors	665/694	210
SQ38	Multiphoton bioimaging	699/713	15
SQ39	*In vitro* imaging of OVCAR-3 cells and *in vivo* imaging of mouse ear vasculature	621/630	216
SQ40	Multiphoton bioimaging of blood flow in mouse brain vessels	560–575/580–600	217
SQ41	High-resolution visualization of HeLa	641/658	218
SQ42	High-resolution visualization of HeLa	679/690	218
SQ43	High-resolution imaging of the liver and tumors	632/700	15
SQ44	Multimodal imaging	940/980	69
SQ45	Multimodal imaging of tumor in mice and photodynamic therapy	665/680	41
SQ46	Multimodal imaging and photothermal therapy	659/673	224
SQ47	NIR imaging and photothermal therapy	882/1290	76
SQ48	Photodynamic therapy (PDT) agent for treating superficial tumors and vascular abnormalities.	—	236
SQ49	PDT agent for treating superficial tumors and vascular abnormalities	—	236
SQ50	Photodynamic therapy agent to treat MCF-7 cancer cells	644/655	237
SQ51	Photodynamic therapy for treatment of HeLa cells	676/699	238
SQ52	Tumour imaging and photodynamic therapy	679/690	239
SQ53	Photothermal therapy on melanoma cells and tumor-xenografted mice	965–1045/1031–1116	81
SQ54	Photothermal therapy	—	223
SQ55	Photothermal therapy in 4T1 tumor-bearing mice	765/800	250
SQ56	Photothermal therapy in 4T1 tumor-bearing mice	780/800	250
SQ57	Targeted drug delivery	—	254

These dyes exhibited high biocompatibility and low cytotoxicity, making them suitable for biomedical applications. Therefore, **SQ55** and **SQ56** are promising PTT agents, offering significant potential for precise and effective cancer treatment through PTT.[250]

Targeted drug delivery

The design of squaraine-based conjugates and nanoparticles for targeted drug delivery is a critical aspect of theranostic applications. These systems are engineered to enhance the specificity and efficacy of drug delivery to tumor sites while minimizing systemic toxicity. Various strategies have been employed to achieve targeted delivery, including the use of ligands that bind specifically to overexpressed receptors on cancer cells.[251]

In a study, it was noted that squaraine encapsulated in mesoporous silica nanoparticles (**SQ29**-MSPN) has applications in targeted drug delivery. **SQ29**-MSPN can be used for controlled intracellular drug/gene co-delivery. It works by functionalizing disulfide bond linked amine groups on **SQ29**-MSPN, thereby an electrostatic interaction takes place between negatively charged sSQNA (model gene) and positively charged ammonium-functionalized **SQ29**-MSPN. Finally, sSQNA-coated nanoparticles (**SQ29**-MSPN -SS-NH3 + + sSQNA) are obtained and the drug will be blocked inside the mesopores. Addition of a reducing agent will cleave the disulphide bond and then the sSQNA and drug were triggered to release from the **SQ29**-MSPN. After the cell uptake, the drug and sSQNA would be released inside the cells, which populate intracellular (glutathione) GSH in the cells, realizing drug/sSQNA co-delivery.[252]

When squaraine dye **SQ57** (Fig. 22) is incorporated into the PAAm hydrogel as a covalent cross-linker, an **SQ57**@PAAm hydrogel gel is obtained, which acts a photothermal therapy agent. It was noted that when methotrexate (MTX) was loaded into the hydrogel as a model drug, MTX release was made possible by irradiating the **SQ57** @PAAm hydrogel.[253] Similarly, **SQ57** @poly(HEMA-*co*-AA) hydrogels have found applications in photodynamic therapy by producing reactive oxygen species under red light and in photothermal therapy by producing hyperthermia under near-infrared light. Notably, **SQ57**@poly(-HEMA-*co*-AA) hydrogels were used as flexible materials for controlled release of drugs, especially in the treatment of skin cancer. The structure of hydrogels enables the loading of rhodamine B inside, which under 808 nm laser irradiation facilitates controlled release of the drug (Table 1).[254]

Conclusions

Squaraine dyes, with their favourable photophysical and photochemical properties, have been proven to be versatile molecular tools in the field of biophotonics (Table 2). The strong and tunable absorption and emission in the NIR region, high fluorescence quantum yields, photostability, and biocompatibility of squaraine dyes enabled their application in various fields ranging from molecular sensing and bioimaging to advanced theranostics. Innovations in structural design, molecular assemblies, nanomaterial conjugation, and encapsulation have eliminated several inherent limitations of squaraine dyes, particularly aggregation in aqueous media and chemical instability, thereby widening their scope for application in biological environments.

In this review, we have discussed how squaraine-based probes have helped in advancing selective and sensitive detection of biorelevant molecules, ions, proteins, and nucleic acids. Squaraine dyes have played an important role in developing advanced multimodal imaging strategies such as NIR fluorescence, multiphoton, and photoacoustic imaging. Furthermore, the dual role of squaraines as diagnostic and therapeutic agents has been discussed, emphasising photodynamic therapy, photothermal therapy, and targeted drug delivery.

Despite many of their favourable features, squaraine dyes still possess several drawbacks such as solubility, long-term biocompatibility, targeted *in vivo* delivery, and large-scale translation into clinical practice. Future research needs to be focused on molecular design to enhance the aqueous solubility and stability of squaraine dyes, their integration with multifunctional nanocarriers, and systematic *in vivo* validation to connect the gap between laboratory discoveries and real-world biomedical applications.

In conclusion, over the years squaraine dyes have evolved from normal fluorescent molecules to multifunctional platforms that played a significant role in diagnostics and therapeutics. Therefore, further developments in squaraine chemistry should focus on shaping the next generation of biophotonic materials and technologies, paving the way for breakthroughs in non-invasive imaging, disease monitoring, and personalized treatment modalities.

Author contributions

A. A. and S. S. conceptualized, supervised, wrote the original draft, and performed reviewing and editing. S. S., C. S. and B. V. performed data collection, validation, writing and editing.

Conflicts of interest

The authors declare no competing interests.

Data availability

No primary research results, software or code have been included and no new data were generated or analysed as part of this review.

Acknowledgements

A. A. is grateful to CSIR, Govt. of India for a CSIR-Bhatnagar Fellowship grant (CSIRHRD/BFS/2024/03/03). S. S. expresses thanks to SRMIST-KTR for support under the SERI grant (No. SERI2024/174/10). C. S. is thankful to SRMIST-KTR for a research fellowship.

Notes and references

1 S. Sreejith, P. Carol, P. Chithra and A. Ajayaghosh, *J. Mater. Chem.*, 2008, **18**, 264–274.
2 J. He, Y. J. Jo, X. Sun, W. Qiao, J. Ok, T. il Kim and Z. Li, *Adv. Funct. Mater.*, 2021, **31**, 2008201.
3 T. Maeda, *Prog. Funct. Dyes Sci.*, 2021, 21–47.
4 A. Treibs and K. Jacob, *Angew. Chem., Int. Ed. Engl.*, 1965, **4**, 694.
5 W. Qiao and Z. Li, *Symmetry*, 2022, **14**, 966.
6 A. Mei, X. He, D. Lei, L. Wang, W. Wang, J. Shao, Q. Shen, F. Jiang and X. Dong, *Coord. Chem. Rev.*, 2025, **527**, 216419.
7 G. Chen, H. Sasabe, T. Igarashi, Z. Hong and J. Kido, *J. Mater. Chem. A*, 2015, **3**, 14517–14534.
8 C. Qin, Y. Numata, S. Zhang, X. Yang, A. Islam, K. Zhang, H. Chen and L. Han, *Adv. Funct. Mater.*, 2014, **24**, 3059–3066.
9 A. K. Singh, M. F. M. Kavungathodi, A. J. Mozer, K. Krishnamoorthy and J. Nithyanandhan, *Langmuir*, 2022, **38**, 14808–14818.
10 K. Strassel, W. H. Hu, S. Osbild, D. Padula, D. Rentsch, S. Yakunin, Y. Shynkarenko, M. Kovalenko, F. Nüesch, R. Hany and M. Bauer, *Sci. Technol. Adv. Mater.*, 2021, **22**, 194–204.
11 B. Pitner, K. J. Thomas, D. B. Sherman, J. Alarcon, G. Mohiuddin, K. S. Kyler and B. R. Venepalli, *Proc. SPIE*, 2005, **5704**, 24–29.
12 J. R. Johnson, N. Fu, E. Arunkumar, W. M. Leevy, S. T. Gammon, D. Piwnica-Worms and B. D. Smith, *Angew. Chem., Int. Ed.*, 2007, **46**, 5528.
13 A. G. White, N. Fu, W. M. Leevy, J. J. Lee, M. A. Blasco and B. D. Smith, *Bioconjug. Chem.*, 2010, **21**, 1297–1304.
14 H. Y. Ahn, S. Yao, X. Wang and K. D. Belfield, *ACS Appl. Mater. Interfaces*, 2012, **4**, 2847–2854.
15 F. F. An, Z. J. Deng, J. Ye, J. F. Zhang, Y. L. Yang, C. H. Li, C. J. Zheng and X. H. Zhang, *ACS Appl. Mater. Interfaces*, 2014, **6**, 17985–17992.
16 P. Sun, Q. Wu, X. Sun, H. Miao, W. Deng, W. Zhang, Q. Fan and W. Huang, *Chem. Commun.*, 2018, **54**, 13395–13398.
17 D. Ramaiah, I. Eckert, K. T. Arun, L. Weidenfeller and B. Epe, *Photochem. Photobiol.*, 2002, **76**, 672–677.
18 F. P. Gao, Y. X. Lin, L. L. Li, Y. Liu, U. Mayerhöffer, P. Spenst, J. G. Su, J. Y. Li, F. Würthner and H. Wang, *Biomaterials*, 2014, **35**, 1004–1014.
19 M. Pamuk Algi and R. Sarıgöl, *Dyes and Pigm.*, 2024, **226**, 112138.
20 H. Xu, L. Cheng, C. Wang, X. Ma, Y. Li and Z. Liu, *Biomaterials*, 2011, **32**, 9364–9373.
21 J. Alkabli, Y. Q. Almulaiky and S. A. Al-horaibi, *Appl. Mater. Today*, 2025, **42**, 102590.
22 L. Hu, Z. Yan and H. Xu, *RSC Adv.*, 2013, **3**, 7667–7676.
23 N. Nizomov, Z. F. Ismailov, S. N. Nizamov, M. K. Salakhitdinova, A. L. Tatarets, L. D. Patsenker and G. Khodjayev, *J. Mol. Struct.*, 2006, **788**, 36–42.
24 T. Liu, X. Liu, W. Wang, Z. Luo, M. Liu, S. Zou, C. Sissa, A. Painelli, Y. Zhang, M. Vengris, M. V. Bondar, D. J. Hagan, E. W. Van Stryland, Y. Fang and K. D. Belfield, *J. Phys. Chem. C*, 2018, **122**, 3994–4008.
25 A. L. Tatarets, I. A. Fedyunyayeva, T. S. Dyubko, Y. A. Povrozin, A. O. Doroshenko, E. A. Terpetschnig and L. D. Patsenker, *Anal. Chim. Acta*, 2006, **570**, 214–223.
26 A. Ajayaghosh, *Acc. Chem. Res.*, 2005, **38**, 449–459.
27 S. Pradhan, Y. Kurokawa, S. Gupta, K. R. B. Singh and S. S. Pandey, *ACS Appl. Energy Mater.*, 2024, **7**, 12004–12015.
28 J. Csucker, E. Didier, J. Pedro Ferreira Assunção, D. Rentsch, R. Kothandaraman, D. Bachmann, I. Shorubalko, F. Nüesch, R. Hany and M. Bauer, *Adv. Sci.*, 2025, **12**, 2502320.
29 G. Chen, H. Sasabe, W. Lu, X. F. Wang, J. Kido, Z. Hong and Y. Yang, *J. Mater. Chem. C*, 2013, **1**, 6547–6552.
30 H. Chen, M. S. Farahat, K. Y. Law and D. G. Whitten, *J. Am. Chem. Soc.*, 1996, **118**, 2584–2594.
31 W. Wang, A. Fu, J. Lan, G. Gao, J. You and L. Chen, *Chem. Eur. J.*, 2010, **16**, 5129–5137.
32 Y. D. Lee, C. K. Lim, S. Kim, I. C. Kwon and J. Kim, *Adv. Funct. Mater.*, 2010, **20**, 2786–2793.
33 Z. Cong, Y. Li, G. Xia, S. Shen, J. Sun, K. Xu, Z. Jiang, L. Jiang, Y. Chen, Q. Yu and H. Wang, *Dyes Pigm.*, 2019, **162**, 654–661.
34 R. R. Avirah, D. T. Jayaram, N. Adarsh and D. Ramaiah, *Org. Biomol. Chem.*, 2012, **10**, 911–920.
35 U. Mayerhöffer, M. Gsänger, M. Stolte, B. Fimmel and F. Würthner, *Chem. Eur. J.*, 2013, **19**, 218–232.
36 G. Alberto, N. Barbero, C. Divieto, E. Rebba, M. P. Sassi, G. Viscardi and G. Martra, *Colloids Surf. A Physicochem. Eng. Asp.*, 2019, **568**, 123–130.
37 S. Singh, W. E. Meador, A. Pramanik, P. Ray, J. H. Delcamp and Y. Zhao, *J. Photochem. Photobiol. B*, 2023, **240**, 112652.
38 C. L. Sun, S. K. Lv, Y. P. Liu, Q. Liao, H. L. Zhang, H. Fu and J. Yao, *J. Mater. Chem. C*, 2017, **5**, 1224–1230.
39 K. Schenke-Layland, *J. Biophotonics*, 2008, **1**, 451–462.
40 P. Beard, *Interface Focus*, 2011, **1**, 602–631.
41 Y. D. Park, J. E. Park, H. S. Kim, S. H. Choi, J. E. Park, J. Jeon and S. H. Park, *Bioconjug. Chem.*, 2020, **31**, 2607–2617.
42 R. Song, Y. Dong, Z. Zhong, Q. Zhao, Y. Hu, M. Lei, P. Lei, Z. Jiang, K. Qian, C. Shi, Z. He, Y. Qin, J. Wang and H. Chen, *J. Med. Chem.*, 2024, **67**, 10275–10292.
43 S. Luo, E. Zhang, Y. Su, T. Cheng and C. Shi, *Biomaterials*, 2011, **32**, 7127–7138.
44 K. Y. Law and F. C. Bailey, *J. Org. Chem.*, 2002, **57**, 3278–3286.
45 K. Y. Law, F. C. Bailey and L. J. Bluett, *Can. J. Chem.*, 1986, **64**, 1607–1619.
46 K. Ilina, W. M. MacCuaig, M. Laramie, J. N. Jeouty, L. R. McNally and M. Henary, *Bioconjug. Chem.*, 2019, **31**, 194–213.
47 F. Meyers, C. T. Chen, S. R. Marder and J. L. Brédas, *Chem. Eur. J.*, 1997, **3**, 530–537.
48 A. M. Della Pelle, P. J. Homnick, Y. Bae, P. M. Lahti and S. Thayumanavan, *J. Phys. Chem. C*, 2014, **118**, 1793–1799.
49 C. Cornelissen-Gude, W. Rettig and R. Lapouyade, *J. Phys. Chem. A*, 1997, **101**, 9673–9677.
50 G. M. Paternò, L. Moretti, A. J. Barker, C. D'Andrea, A. Luzio, N. Barbero, S. Galliano, C. Barolo, G. Lanzani and F. Scotognella, *J. Mater. Chem. C*, 2017, **5**, 7732–7738.

51 M. Kasha, *Discuss. Faraday Soc.*, 1950, **9**, 14–19.
52 L. Yu, X. Liu, S. Zhao, W. Zhu, L. Wu and C. Ding, *Appl. Spectrosc.*, 2024, **78**, 974–981.
53 S. Alex, M. C. Basheer, K. T. Arun, D. Ramaiah and S. Das, *J. Phys. Chem. A*, 2007, **111**, 3226–3230.
54 G. M. Paternò, L. Moretti, A. J. Barker, C. D'Andrea, A. Luzio, N. Barbero, S. Galliano, C. Barolo, G. Lanzani and F. Scotognella, *J. Mater. Chem. C*, 2017, **5**, 7732–7738.
55 G. Chen, H. Sasabe, W. Lu, X.-F. Wang, J. Kido, Z. Hong and Y. Yang, *J. Mater. Chem. C*, 2013, **1**, 6547–6552.
56 Z. Yan, H. Xu, S. Guang, X. Zhao, W. Fan and X. Y. Liu, *Adv. Funct. Mater.*, 2012, **22**, 345–352.
57 T. Liu, X. Liu, Y. Zhang, M. V. Bondar, Y. Fang and K. D. Belfield, *Eur. J. Org. Chem.*, 2018, 4095–4102.
58 E. Arunkumar, C. C. Forbes, B. C. Noll and B. D. Smith, *J. Am. Chem. Soc.*, 2005, **127**, 3288–3289.
59 E. Arunkumar, N. Fu and B. D. Smith, *Chem. Eur. J.*, 2006, **12**, 4684–4690.
60 S. Sreejith, J. Joseph, M. Lin, N. V. Menon, P. Borah, H. J. Ng, Y. X. Loong, Y. Kang, S. W. K. Yu and Y. Zhao, *ACS Nano*, 2015, **9**, 5695–5704.
61 S. Dong, J. D. W. Teo, L. Y. Chan, C. L. K. Lee and K. Sou, *ACS Appl. Nano Mater.*, 2018, **1**, 1009–1013.
62 D. Bagchi, A. Halder, S. Debnath, P. Saha and S. Kumar Pal, *J. Photochem. Photobiol. A Chem.*, 2019, **380**, 111842.
63 P. Anees, S. Sreejith and A. Ajayaghosh, *J. Am. Chem. Soc.*, 2014, **136**, 13233–13239.
64 J. J. McEwen and K. J. Wallace, *Chem. Commun.*, 2009, 6339–6351.
65 K. Ilina, W. M. Maccuaig, M. Laramie, J. N. Jeouty, L. R. Mcnally and M. Henary, *Bioconj. Chem.*, 2020, **31**, 194–213.
66 W. Qiao and Z. Li, *Symmetry*, 2022, **14**, 966.
67 G. Xia and H. Wang, *J. Photochem. Photobiol. C: Photochem. Rev.*, 2017, **31**, 84–113.
68 L. Beverina and P. Salice, *Eur. J. Org. Chem.*, 2010, 1207–1225.
69 D. Yao, Y. Wang, R. Zou, K. Bian, P. Liu, S. Shen, W. Yang, B. Zhang and D. Wang, *ACS Appl. Mater. Interfaces*, 2020, **12**, 4276–4284.
70 S. Kuster and T. Geiger, *Dyes and Pigm.*, 2012, **95**, 657–670.
71 S. N. Nizamov, M. N. Barakaeva, E. N. Kurtaliev, A. L. Tatarets and L. D. Patsenker, *J. Appl. Spectrosc.*, 2009, **76**, 464–469.
72 D. D. S. Pisoni, M. P. De Abreu, C. L. Petzhold, F. S. Rodembusch and L. F. Campo, *J. Photochem. Photobiol. A Chem.*, 2013, **252**, 77–83.
73 Y. Zhang, B. Kim, S. Yao, M. V. Bondar and K. D. Belfield, *Langmuir*, 2013, **29**, 11005–11012.
74 S. Luo, E. Zhang, Y. Su, T. Cheng and C. Shi, *Biomaterials*, 2011, **32**, 7127–7138.
75 K. Umezawa, D. Citterio and K. Suzuki, *Anal. Sci.*, 2014, **30**, 327–349.
76 W. Zhang, W. Deng, H. Zhang, X. Sun, T. Huang, W. Wang, P. Sun, Q. Fan and W. Huang, *Biomaterials*, 2020, **243**, 119934.
77 M. Manley, *Chem. Soc. Rev.*, 2014, **43**, 8200–8214.
78 S. Khopkar and G. Shankarling, *Dyes and Pigm.*, 2019, **24**, 1.
79 P. K. Upputuri and M. Pramanik, *J. Biomed. Opt.*, 2019, **24**, 1.
80 L. Yuan, W. Lin, S. Zhao, W. Gao, B. Chen, L. He and S. Zhu, *J. Am. Chem. Soc.*, 2012, **134**, 13510–13523.
81 Y. Wang, G. Xia, J. Wang, M. Wang, W. Guo, M. Tan, L. Si, Y. Yang, H. Wang and H. Wang, *Sci. China Chem.*, 2024, **67**, 612–621.
82 X. Li, S. Guo, W. Deng, S. Wu, P. Sun and Y. Liu, *J. Mater. Chem. B*, 2023, **11**, 4389–4395.
83 S. Das, K. G. Thomas, P. V. Kamat and M. V. George, *J. Chem. Sci.*, 1993, **105**, 513–525.
84 G. Chen, D. Yokoyama, H. Sasabe, Z. Hong, Y. Yang and J. Kido, *Appl. Phys. Lett.*, 2012, **105**, 513–525.
85 S. Gupta, Y. Yamawaki, S. Pradhan, S. S. Pandey and T. Kato, *Phys. Status Solidi A*, 2023, **220**, 2300226.
86 L. I. Markova, E. A. Terpetschnig and L. D. Patsenker, *Dyes and Pigm.*, 2013, **99**, 561–570.
87 L. V. Wang and S. Hu, *Science*, 2012, **335**, 1458–1462.
88 D. Zhang, Y. X. Zhao, Z. Y. Qiao, U. Mayerhöffer, P. Spenst, X. J. Li, F. Würthner and H. Wang, *Bioconjug. Chem.*, 2014, **25**, 2021–2029.
89 J. M. Fernandez, M. D. Bilgin and L. I. Grossweiner, *J. Photochem. Photobiol. B*, 1997, **37**, 131–140.
90 E. Lima and L. V. Reis, *Future Med. Chem.*, 2022, **14**, 1375–1402.
91 D. Ramaiah, A. Joy, N. Chandrasekhar, N. V. Eldho, S. Das and M. V. George, *Photochem. Photobiol.*, 1997, **65**, 783–790.
92 B. Li, L. Lin, H. Lin and B. C. Wilson, *J. Biophotonics*, 2016, **9**, 1314–1325.
93 X. Chen, X. Ma, G. Yang, G. Huang, H. Dai, N. Liu and J. Yu, *Nanophotonics*, 2023, **12**, 3645–3652.
94 P. Salice, J. Arnbjerg, B. W. Pedersen, R. Toftegaard, L. Beverina, G. A. Pagani and P. R. Ogilby, *J. Phys. Chem. A*, 2010, **114**, 2518–2525.
95 M. Oheim, D. J. Michael, M. Geisbauer, D. Madsen and R. H. Chow, *Adv. Drug Deliv. Rev.*, 2006, **58**, 788–808.
96 M. V. Bondar, S. Faryadras, N. Munera, H. J. Chang, M. Uddin, K. D. Belfield, O. D. Kachkovsky, E. W. Van Stryland and D. J. Hagan, *J. Phys. Chem. B*, 2022, **126**, 3897–3907.
97 Y. Li, T. Liu, H. Liu, M. Z. Tian and Y. Li, *Acc. Chem. Res.*, 2014, **47**, 1186–1198.
98 D. D. Ta and S. V. Dzyuba, *Chemosensors*, 2021, **9**, 302.
99 A. S. Klymchenko, *Acc. Chem. Res.*, 2017, **50**, 366–375.
100 L. Tang, S. Sharma and S. S. Pandey, *Molecules*, 2022, **27**, 6578.
101 J. Griffiths and J. Mama, *Dyes and Pigm.*, 1999, **44**, 9–17.
102 L. Xue, B. Li, Q. Fei, G. Feng, Y. Huan and Z. Shi, *Nanotechnology*, 2010, **21**, 215502.
103 P. Anees, K. V. Sudheesh, P. Jayamurthy, A. R. Chandrika, R. V. Omkumar and A. Ajayaghosh, *Chem. Sci.*, 2016, **7**, 6808–6814.
104 M. Sameiro and T. Gonçalves, *Chem. Rev.*, 2009, **109**, 190–212.
105 O. A. Mass, C. K. Wilson, G. Barcenas, E. A. Terpetschnig, O. M. Obukhova, O. S. Kolosova, A. L. Tatarets, L. Li,

B. Yurke, W. B. Knowlton, R. D. Pensack and J. Lee, *J. Phys. Chem. C*, 2022, **126**, 3475–3488.
106 L. Beverina and P. Salice, *Eur. J. Org. Chem.*, 2010, 1207–1225.
107 C. Eggeling, J. Widengren, R. Rigler and C. A. M. Seidel, *Anal. Chem.*, 1998, **70**, 2651–2659.
108 M. Lu, Y. Zhang, B. Li, X. Li, S. Xu, Z. Li and B. Yang, *J. Mater. Sci.: Mater. Electron.*, 2018, **29**, 12856–12870.
109 D. P. Ferreira, D. S. Conceição, V. R. A. Ferreira, V. C. Graça, P. F. Santos and L. F. V. Ferreira, *Photochem. Photobiol. Sci.*, 2013, **12**, 1948–1959.
110 B. Zhao, D. Guan, J. Liu, X. Zhang, S. Xiao, Y. Zhang, B. D. Smith and Q. Liu, *Nano Lett*, 2024, **24**, 4944.
111 S. Das, K. G. Thomas and M. V. George, *Org. Photochem.*, 1997, 467–518.
112 G. Renno, F. Cardano, V. Ilieva, G. Viscardi and A. Fin, *Eur. J. Org. Chem.*, 2022, e202200833.
113 J. T. Alander, I. Kaartinen, A. Laakso, T. Pätilä, T. Spillmann, V. V. Tuchin, M. Venermo and P. Välisuo, *Int. J. Biomed. Imaging*, 2012, **2012**, 940585.
114 V. Sabapathy, J. Mentam, P. M. Jacob and S. Kumar, *Stem Cells Int.*, 2015, **2015**, 606415.
115 R. B. Mujumdar, L. A. Ernst, S. R. Mujumdar and C. J. Lewis, *Bioconjug. Chem.*, 2002, **13**, 105–111.
116 M. Ünlü, M. E. Morgan and J. S. Minden, *Electrophoresis*, 1997, **18**, 2071–2077.
117 A. P. Yuen, S. M. Jovanovic, A. M. Hor, R. A. Klenkler, G. A. Devenyi, R. O. Loutfy and J. S. Preston, *Sol. Energy*, 2012, **86**, 1683–1688.
118 F. Ghani, J. Kristen and H. Riegler, *J. Chem. Eng. Data*, 2012, **57**, 439–449.
119 H. Lu, J. MacK, Y. Yang and Z. Shen, *Chem. Soc. Rev.*, 2014, **43**, 4778–4823.
120 A. Schmitt, B. Hinkeldey, M. Wild and G. Jung, *J. Fluoresc.*, 2008, **19**, 755–758.
121 S. I. Sohn, A. Priya, B. Balasubramaniam, P. Muthuramalingam, C. Sivasankar, A. Selvaraj, A. Valliammai, R. Jothi and S. Pandian, *Pharmaceutics*, 2021, **13**, 2102.
122 S. Mondal, S. Ghosh and S. P. Moulik, *J. Photochem. Photobiol., B*, 2016, **158**, 212–218.
123 Z. Tao, G. Hong, C. Shinji, C. Chen, S. Diao, A. L. Antaris, B. Zhang, Y. Zou and H. Dai, *Angew. Chem., Int. Ed.*, 2013, **52**, 13002–13006.
124 G. Hong, Y. Zou, A. L. Antaris, S. Diao, D. Wu, K. Cheng, X. Zhang, C. Chen, B. Liu, Y. He, J. Z. Wu, J. Yuan, B. Zhang, Z. Tao, C. Fukunaga and H. Dai, *Nat. Commun.*, 2014, **5**, 4206.
125 Y. Sun, C. Qu, H. Chen, M. He, C. Tang, K. Shou, S. Hong, M. Yang, Y. Jiang, B. Ding, Y. Xiao, L. Xing, X. Hong and Z. Cheng, *Chem. Sci.*, 2016, **7**, 6203–6207.
126 B. Li, L. Lu, M. Zhao, Z. Lei and F. Zhang, *Angew. Chem., Int. Ed.*, 2018, **57**, 7483–7487.
127 A. L. Antaris, H. Chen, K. Cheng, Y. Sun, G. Hong, C. Qu, S. Diao, Z. Deng, X. Hu and B. Zhang, *Nat. Mater.*, 2016, **15**, 235–242.
128 L. Li, S. Diao, R. Ma, A. Nguyen, G. Hong, Z. Ma, J. Wang, S. Zhu, J. M. Castellano and T. Wyss-Coray, *Adv. Mater.*, 2016, **28**, 318–323.
129 Q. Yang, Z. Ma, H. Wang, B. Zhou, S. Zhu, Y. Zhong, J. Wang, H. Wan, A. L. Antaris, R. Ma, X. Zhang, J. Yang, X. Zhang, H. Sun, W. Liu, Y. Liang and H. Dai, *Adv. Mater.*, 2017, **29**, 1605497.
130 S. Zhu, S. Herraiz, J. Yue, M. Zhang, H. Wan, Q. Yang, Z. Ma, Y. Wang, J. He, A. L. Antaris, Y. Zhong, S. Diao, Y. Feng, Y. Zhou, K. Yu, G. Hong, Y. Liang, A. J. Hsueh and H. Dai, *Adv. Mater.*, 2018, **30**, 1705799.
131 S. Zhu, Q. Yang, A. L. Antaris, J. Yue, Z. Ma, H. Wang, W. Huang, H. Wan, J. Wang, S. Diao, B. Zhang, X. Li, Y. Zhong, K. Yu, G. Hong, J. Luo, Y. Liang and H. Dai, *Proc. Natl. Acad. Sci. U. S. A.*, 2017, **114**, 962–967.
132 Q. Yang, Z. Hu, S. Zhu, R. Ma, H. Ma, Z. Ma, H. Wan, T. Zhu, Z. Jiang, W. Liu, L. Jiao, H. Sun, Y. Liang and H. Dai, *J. Am. Chem. Soc.*, 2018, **140**, 1715–1724.
133 C. Deibe, T. Strobe and V. Dyakonov, *Adv. Mater.*, 2010, **22**, 4097–4111.
134 Y. Li, B. Xu, P. Song, F. Ma and M. Sun, *J. Phys. Chem. C*, 2017, **121**, 12546–12561.
135 A. Ajayaghosh, *Chem. Soc. Rev.*, 2003, **32**, 181–191.
136 X. Tian, L. C. Murfin, L. Wu, S. E. Lewis and T. D. James, *Chem. Sci.*, 2021, **12**, 3406–3426.
137 D. Escudero, *Acc. Chem. Res.*, 2016, **49**, 1816–1824.
138 E. Arunkumar and A. Ajayaghosh, *Chem. Commun.*, 2005, 599–601.
139 M. J. Paterson, L. Blancafort, S. Wilsey and M. A. Robb, *J. Phys. Chem. A*, 2002, **106**, 11431–11439.
140 Sushma, S. Sharma and K. S. Ghosh, *Crit. Rev. Anal. Chem.*, 2024, 1–32.
141 H. Yu, M. Fu and Y. Xiao, *Phys. Chem. Chem. Phys.*, 2010, **12**, 7386–7391.
142 T. Maujean, P. Wagner, C. Valencia, S. Riché, X. Iturrioz, P. Villa, N. Girard, J. Karpenko, M. Gulea and D. Bonnet, *Bioconjug. Chem.*, 2022, **34**, 162–168.
143 Y. Dong, A. Iagatti, P. Foggi, J. Zhao, G. Mazzone, K. Xu, W. Ji, M. Di Donato and N. Russo, *Dyes and Pigm.*, 2017, **147**, 560–572.
144 B. Ostwald, F. Lehmann, L. Simon, E. Terpetschnig and O. S. Wolfbeis, *Anal. Biochem.*, 2000, **280**, 272–277.
145 L. Yuan, W. Lin, K. Zheng and S. Zhu, *Acc. Chem. Res.*, 2013, **46**, 1462–1473.
146 J. M. Favret and S. V. Dzyuba, *Molecules*, 2024, **30**, 116.
147 G. Wang, X. Jiang and N. Fu, *Dyes and Pigm.*, 2019, **171**, 107698.
148 Y. Xu, A. Malkovskiy, Q. Wang and Y. Pang, *Org. Biomol. Chem.*, 2011, **9**, 2878–2884.
149 R. Feng, Y. Xu, H. Zhao, X. Duan and S. Sun, *Analyst*, 2016, **141**, 36–53.
150 D. S. Philips, S. Ghosh, K. V. Sudheesh, C. H. Suresh and A. Ajayaghosh, *Chem. Eur. J.*, 2017, **23**, 17973–17980.
151 W. Zhu, S. Zhao, B. Yu, Y. Tao, C. Wang, L. Shi, X. Zhang, J. Meng, C. Wu, C. Ding and L. Yu, *Anal. Sci.*, 2025, **41**, 289–296.
152 S. Sreejith, K. P. Divya and A. Ajayaghosh, *Angew. Chem., Int. Ed*, 2008, **47**, 7883–7887.
153 P. Anees, J. Joseph, S. Sreejith, N. V. Menon, Y. Kang, S. Wing-Kwong Yu, A. Ajayaghosh and Y. Zhao, *Chem. Sci.*, 2016, **7**, 4110–4116.

154 R. Hu, G. Zhang, A. Qin and B. Z. Tang, *Pure and Appl. Chem.*, 2021, **93**, 1383–1402.
155 M. Hui Chua, H. Zhou, T. Ting Lin, J. Wu and J. Xu, *ACS Omega*, 2018, **3**, 16424–16435.
156 T. Zou, Y. Chen, S. He, H. Huang, Z. Yuwen, D. Zhang, L. Zhang and H. Liu, *Nano Today*, 2015, **65**, 102869.
157 D. M. Kong, *Methods*, 2013, **64**, 199–204.
158 B. Jin, X. Zhang, W. Zheng, X. Liu, J. Zhou, N. Zhang, F. Wang and D. Shangguan, *Anal. Chem.*, 2014, **86**, 7063–7070.
159 Y. Guo, Y. Chen, X. Zhu, Z. Pan, X. Zhang, J. Wang and N. Fu, *Sens. Actuators B Chem*, 2018, **255**, 977–985.
160 G. Wang, W. Xu, Y. Guo and N. Fu, *Sens. Actuators B Chem.*, 2017, **245**, 932–937.
161 B. L. Renard, Y. Aubert and U. Asseline, *Tetrahedron Lett.*, 2009, **50**, 1897–1901.
162 B. Wu, Y. Lin, B. Li, C. Zhan, F. Zeng and S. Wu, *Anal. Chem.*, 2018, **90**, 9359–9365.
163 S. K. Mavileti, G. Bila, V. Utka, R. Bilyy, E. Bila, E. Butoi, S. Gupta, P. Balyan, T. Kato, R. Bilyy and S. S. Pandey, *ACS Appl. Mater. Interfaces*, 2025, **17**, 9140–9154.
164 A. Barnado, L. J. Crofford and J. C. Oates, *J. Leukoc. Biol*, 2016, **99**, 265–278.
165 A. Ajayaghosh, E. Arunkumar and J. Daub, *Angew. Chem., Int. Ed.*, 2002, **41**, 1766–1769.
166 E. Arunkumar, A. Ajayaghosh and J. Daub, *J. Am. Chem. Soc.*, 2005, **127**, 3156–3164.
167 M. C. Linder and M. Hazegh-Azam, *Am. J. Clin. Nutr.*, 1996, **63**, 797S–811S.
168 R. Uauy, M. Olivares and M. Gonzalez, *Am. J. Clin. Nutr.*, 1998, **67**, 952S–959S.
169 R. Krämer, *Angew. Chem., Int. Ed.*, 1998, **37**, 772–773.
170 W. Wang, A. Fu, J. You, G. Gao, J. Lan and L. Chen, *Tetrahedron*, 2010, **66**, 3695–3701.
171 X. Zhu, Q. Zheng, G. Wang and N. Fu, *Sens. Actuators B Chem.*, 2016, **237**, 802–809.
172 K. Boonkitpatarakul, J. Wang, N. Niamnont, B. Liu, L. McDonald, Y. Pang and M. Sukwattanasinitt, *ACS Sens.*, 2015, **1**, 144–150.
173 M. Mukherjee, S. Pal, S. Lohar, B. Sen, S. Sen, S. Banerjee, S. Banerjee and P. Chattopadhyay, *Analyst*, 2014, **139**, 4828–4835.
174 I. H. Hwang, Y. W. Choi, K. B. Kim, G. J. Park, J. J. Lee, L. T. Nguyen, I. Noh and C. Kim, *New J. Chem.*, 2016, **40**, 171–178.
175 J. Sun, Y. Li, S. Shen, Q. Yan, G. Xia and H. Wang, *Spectrochim. Acta A Mol. Biomol. Spectrosc.*, 2020, **228**, 117590.
176 P. B. Tchounwou, W. K. Ayensu, N. Ninashvili and D. Sutton, *Environ. Toxicol.*, 2003, **18**, 149–175.
177 H. H. Harris, I. J. Pickering and G. N. George, *Science*, 2003, **301**, 1203.
178 G. Wang, W. Xu, H. Yang and N. Fu, *Dyes and Pigm.*, 2018, **157**, 369–376.
179 G. Wang, W. Xu, Y. Liu and N. Fu, *Microchem. J.*, 2022, **179**, 107481.
180 D. Yur, R. M. Lieser, M. O. Sullivan and W. Chen, *Curr. Opin. Biotechnol.*, 2021, **71**, 41–48.
181 X. Jiang, L. Rong, J. Cao and N. Fu, *Dyes and Pigm.*, 2021, **191**, 109375.
182 Priyanka, G. Bila, S. K. Mavileti, E. Bila, N. Negrych, S. Gupta, L. Tang, R. Bilyy, S. S. Pandey and T. Kato, *Mater. Adv.*, 2024, **5**, 3940–3949.
183 S. K. Mavileti, G. Bila, V. Utka, E. Bila, T. Kato, R. Bilyy and S. S. Pandey, *ACS Appl. Bio Mater.*, 2024, **7**, 416–428.
184 L. Yuan, W. Lin, K. Zheng, L. He and W. Huang, *Chem. Soc. Rev.*, 2013, **42**, 622–661.
185 Z. Hu, W. H. Chen, J. Tian and Z. Cheng, *Trends Mol. Med.*, 2020, **26**, 469–482.
186 X. M. Yi, F. L. Wang, W. J. Qin, X. J. Yang and J. L. Yuan, *Int. J. Nanomed.*, 2014, **9**, 1347–1365.
187 Y. Lin, L. Sun, F. Zeng and S. Wu, *Chem. Eur. J.*, 2019, **25**, 16740–16747.
188 Y. Zheng, H. Yang, H. Wang, K. Kang, W. Zhang, G. Ma and S. Du, *Ann. Transl. Med.*, 2019, **7**, S6.
189 T. Nagaya, Y. A. Nakamura, P. L. Choyke and H. Kobayashi, *Front. Oncol.*, 2017, **7**, 314.
190 R. Solidoro, A. Centonze, M. Miciaccia, O. M. Baldelli, D. Armenise, S. Ferorelli, M. G. Perrone and A. Scilimati, *Med. Res. Rev.*, 2024, **44**, 1800–1866.
191 T. Fukuda, S. Yokomizo, S. Casa, H. Monaco, S. Manganiello, H. Wang, X. Lv, A. D. Ulumben, C. Yang, M. W. Kang, K. Inoue, M. Fukushi, T. Sumi, C. Wang, H. Kang, K. Bao, M. Henary, S. Kashiwagi and H. Soo Choi, *Angew. Chem., Int. Ed.*, 2022, **61**, e202117330.
192 W. E. Meador, S. A. Autry, R. N. Bessetti, J. N. Gayton, A. S. Flynt, N. I. Hammer and J. H. Delcamp, *J. Org. Chem.*, 2020, **85**, 4089–4095.
193 L. Chen, L. Wu, J. Yu, C.-T. Kuo, T. Jian, I.-C. Wu, Y. Rong and D. T. Chiu, *Chem. Sci.*, 2017, **8**, 7236–7245.
194 J. J. Gassensmith, J. M. Baumes and B. D. Smith, *Chem. Commun.*, 2009, 6329–6338.
195 M. S. Barclay, C. K. Wilson, S. K. Roy, O. A. Mass, O. M. Obukhova, R. P. Svoiakov, A. L. Tatarets, A. U. Chowdhury, J. S. Huff, D. B. Turner, P. H. Davis, E. A. Terpetschnig, B. Yurke, W. B. Knowlton, J. Lee and R. D. Pensack, *ChemPhotoChem*, 2022, **6**, e202200039.
196 N. H. Evans, *Eur. J. Org. Chem.*, 2019, 3320–3343.
197 J. M. Baumes, I. Murgu, A. Oliver and B. D. Smith, *Org. Lett.*, 2010, **12**, 4982–4983.
198 S. Y. Hsueh, C. C. Lai, Y. H. Liu, Y. Wang, S. M. Peng and S. H. Chiu, *Org. Lett.*, 2007, **9**, 4523–4526.
199 E. Arunkumar, C. C. Forbes, B. C. Noll and B. D. Smith, *J. Am. Chem. Soc.*, 2005, **127**, 3288–3289.
200 J. Y. Lau, K. Shi, A. G. Oliver and B. D. Smith, *Org. Lett.*, 2025, **27**, 8083–8087.
201 K. Kniazev, T. Guo, C. Zhai, R. S. Gamage, S. Ghonge, P. A. Frantsuzov, M. Kuno and B. Smith, *Dyes and Pigm.*, 2023, **210**, 111031.
202 J. J. Gassensmith, E. Arunkumar, L. Barr, J. M. Baumes, K. M. DiVittorio, J. R. Johnson, B. C. Noll and B. D. Smith, *J. Am. Chem. Soc.*, 2007, **129**, 15054–15059.
203 R. S. Das, P. C. Saha, N. Sepay, A. Mukherjee, S. Chatterjee and S. Guha, *Org. Lett.*, 2020, **22**, 5839–5843.

204 S. Sreejith, X. Ma and Y. Zhao, *J. Am. Chem. Soc.*, 2012, **134**, 17346–17349.
205 L. Yu, X. Fan, H. Zhao, C. Ding, Y. Zhang, J. Fan and X. Tang, *Dyes and Pigm.*, 2022, **206**, 110600.
206 A. Hellebust and R. Richards-Kortum, *Nanomed.*, 2012, **7**, 429–445.
207 J. B. Bomanji, D. C. Costa and P. J. Ell, *Lancet Oncol.*, 2001, **2**, 157–164.
208 Y. Chen, Y. Li, X. Gao and M. Cui, *Dyes and Pigm.*, 2023, **208**, 110822.
209 Y. Wang, M. Wang, G. Xia, Y. Yang, L. Si, H. Wang and H. Wang, *Chem. Commun.*, 2023, **59**, 3598–3601.
210 C. L. Schreiber, C. Zhai, J. M. Dempsey, H. H. McGarraugh, B. P. Matthews, C. R. Christmann and B. D. Smith, *Bioconjug. Chem.*, 2019, **31**, 214–223.
211 J. Sanderson, *Curr. Protoc.*, 2023, **3**, e634.
212 G. S. He, L. S. Tan, Q. Zheng and P. N. Prasad, *Chem. Rev.*, 2008, **108**, 1245–1330.
213 M. E. Dickinson, E. Simbuerger, B. Zimmermann, C. W. Waters and S. E. Fraser, *J. Biomed. Opt.*, 2003, **8**, 329–338.
214 H. Mojzisova and J. Vermot, *Curr. Opin. Genet. Dev.*, 2011, **21**, 549–557.
215 W. R. Zipfel, R. M. Williams and W. W. Webb, *Nat. Biotechnol.*, 2003, **21**, 1369–1377.
216 P. Das, Y. Zhao, R. Yi, J. Song, J. Qu, Y. He, R. Hu, L. Hong, B. Shen, L. Liu, F. Lin and Z. Yang, *Opt. Express*, 2019, **27**, 12360–12372.
217 C. L. Sun, Q. Liao, T. Li, J. Li, J. Q. Jiang, Z. Z. Xu, X. D. Wang, R. Shen, D. C. Bai, Q. Wang, S. X. Zhang, H. B. Fu and H. L. Zhang, *Chem. Sci.*, 2014, **6**, 761–769.
218 H. J. Chang, M. V. Bondar, T. Liu, X. Liu, S. Singh, K. D. Belfield, A. Sheely, A. E. Masunov, D. J. Hagan and E. W. Van Stryland, *ACS Omega*, 2019, **4**, 14669–14679.
219 X. Wang, B. Cui, Q. Sun, H. Liu and Z. Liu, *Chem. Soc. Rev.*, 2025, **54**, 8809–8844.
220 A. B. E. Attia, G. Balasundaram, M. Moothanchery, U. S. Dinish, R. Bi, V. Ntziachristos and M. Olivo, *Photoacoustics*, 2019, **16**, 100144.
221 C. Li, C. Liu, Y. Fan, X. Ma, Y. Zhan, X. Lu and Y. Sun, *RSC Chem. Biol.*, 2021, **2**, 743.
222 H. J. Knox and J. Chan, *Acc. Chem. Res.*, 2018, **51**, 2897–2905.
223 C. He, J. Zhu, H. Zhang, R. Qiao and R. Zhang, *Biosensors*, 2022, **12**, 947.
224 R. S. Das, D. Maiti, S. Kar, T. Bera, A. Mukherjee, P. C. Saha, A. Mondal and S. Guha, *J. Am. Chem. Soc.*, 2023, **145**, 20451–20461.
225 B. J. Burkett, D. J. Bartlett, P. W. McGarrah, A. R. Lewis, D. R. Johnson, K. Berberoğlu, M. K. Pandey, A. T. Packard, T. R. Halfdanarson, C. B. Hruska, G. B. Johnson and A. T. Kendi, *Radiol. Imaging Cancer*, 2023, **5**, e220157.
226 N. Jokar, I. Velikyan, H. Ahmadzadehfar, S. J. Rekabpour, E. Jafari, H. H. Ting, H. J. Biersack and M. Assadi, *Clin. Nucl. Med.*, 2021, **46**, E410–E420.
227 Y. Cai, W. Si, W. Huang, P. Chen, J. Shao and X. Dong, *Small*, 2018, **14**, 1704247.
228 H. Peng, X. Liu, G. Wang, M. Li, K. M. Bratlie, E. Cochran and Q. Wang, *J. Mater. Chem. B*, 2015, **3**, 6856–6870.
229 Y. Park, M. H. Park and H. Hyun, *Int. J. Mol. Sci.*, 2024, **25**, 3428.
230 A. D. Quartarolo, E. Sicilia and N. Russo, *J. Chem. Theory Comput.*, 2009, **5**, 1849–1857.
231 S. Kwiatkowski, B. Knap, D. Przystupski, J. Saczko, E. Kędzierska, K. Knap-Czop, J. Kotlińska, O. Michel, K. Kotowski and J. Kulbacka, *Biomed. Pharmacother.*, 2018, **106**, 1098–1107.
232 D. Sharma, S. Singh, P. Kumar, G. K. Jain, G. Aggarwal, W. H. Almalki and P. Kesharwani, *Nanomater. Photodynamic Ther.*, 2023, 41–54.
233 D. M. Dereje, A. García, C. Pontremoli, B. González, M. Colilla, M. Vallet-Regí, I. Izquierdo-Barba and N. Barbero, *Micropor. Mesopor. Mat.*, 2024, **372**, 113096.
234 G. Feng, G. Q. Zhang and D. Ding, *Chem. Soc. Rev.*, 2020, **49**, 8179–8234.
235 X. Wang, J. Peng, C. Meng and F. Feng, *Chem. Sci.*, 2024, **15**, 12234–12257.
236 D. Ramaiah, I. Eckert, K. T. Arun, L. Weidenfeller and B. Epe, *Photochem. Photobiol.*, 2004, **79**, 99–104.
237 N. Bordignon, M. Köber, G. Chinigò, C. Pontremoli, E. Sansone, G. Vargas-Nadal, M. J. Moran Plata, A. Fiorio Pla, N. Barbero, J. Morla-Folch and N. Ventosa, *Pharmaceutics*, 2023, **15**, 902.
238 D. P. Ferreira, D. S. Conceição, F. Fernandes, T. Sousa, R. C. Calhelha, I. C. F. R. Ferreira, P. F. Santos and L. F. Vieira Ferreira, *J. Phys. Chem. B*, 2016, **120**, 1212–1220.
239 E. Lima, R. E. Boto, D. Ferreira, J. R. Fernandes, P. Almeida, L. F. V. Ferreira, E. B. Souto, A. M. Silva and L. V. Reis, *Materials*, 2020, **13**, 2646.
240 E. Arunkumar, P. K. Sudeep, P. V. Kamat, B. C. Noll and B. D. Smith, *New J. Chem.*, 2007, **31**, 677–683.
241 A. Yuan, J. Wu, X. Tang, L. Zhao, F. Xu and Y. Hu, *J. Pharm. Sci.*, 2013, **102**, 6–28.
242 L. Zhao, X. Zhang, X. Wang, X. Guan, W. Zhang and J. Ma, *J. Nanobiotechnology*, 2021, **19**, 1–15.
243 Y. Chen, L. Li, W. Chen, H. Chen and J. Yin, *Chin. Chem. Lett.*, 2019, **30**, 1353–1360.
244 B. Zhou, Y. Li, G. Niu, M. Lan, Q. Jia and Q. Liang, *ACS Appl. Mater. Interfaces*, 2016, **8**, 29899–29905.
245 N. Eyvazzadeh, A. Shakeri-Zadeh, R. Fekrazad, E. Amini, H. Ghaznavi and S. Kamran Kamrava, *Lasers Med. Sci.*, 2017, **32**, 1469–1477.
246 W. Yang, H. Liang, S. Ma, D. Wang and J. Huang, *Sustain. Mater. Technol.*, 2019, **22**, e00109.
247 X. Ji, R. Shao, A. M. Elliott, R. Jason Stafford, E. Esparza-Coss, J. A. Bankson, G. Liang, Z. P. Luo, K. Park, J. T. Markert and C. Li, *J. Phys. Chem. C*, 2007, **111**, 6245–6251.
248 S. Y. Lee and M. J. Shieh, *ACS Appl. Mater. Interfaces*, 2020, **12**, 4254–4264.

249 W. Qiao, T. Ma, G. Xie, J. Xu, Z. R. Yang, C. Zhong, H. Jiang, J. Xia, L. Zhang, J. Zhu and Z. Li, *ACS Nano*, 2024, **18**, 25671–25684.
250 Y. Yao, Y. Zhang, J. Zhang, X. Yang, D. Ding, Y. Shi, H. Xu and X. Gao, *ACS Appl. Mater. Interfaces*, 2022, **14**, 19192–19203.
251 M. P. Algi and R. Sarigöl, *Mugla J. Sci. and Technol*, 2024, **10**, 120–127.
252 E. Lima, O. Ferreira, R. E. Boto, J. R. Fernandes, P. Almeida, S. M. Silvestre, A. O. Santos and L. V. Reis, *Eur. J. Med. Chem.*, 2025, **293**, 117699.
253 N. Pairault, R. Barat, I. Tranoy-Opalinski, B. Renoux, M. Thomas and S. Papot, *C. R. Chimie*, 2016, **19**, 103–112.
254 X. Ma, H. Feng, C. Liang, X. Liu, F. Zeng and Y. Wang, *J. Mater. Sci. Technol.*, 2017, **33**, 1067–1074.